A MARINE DEEP SEISMIC SOUNDING SURVEY IN THE REGION OF EXPLORER RIDGE

by

STEVEN JEROME MALECEK

B.A., Southwest Minnesota State College, 1973

A THESIS SUBMITTED IN PARTIAL FULFILLMENT OF
THE REQUIREMENTS FOR THE DEGREE OF
MASTER OF SCIENCE

in the Department of
GEOPHYSICS AND ASTRONOMY

We accept this thesis as conforming
to the required standard

THE UNIVERSITY OF BRITISH COLUMBIA

January, 1976

In presenting this thesis in partial fulfilment of the requirements for an advanced degree at the University of British Columbia, I agree that the Library shall make it freely available for reference and study. I further agree that permission for extensive copying of this thesis for scholarly purposes may be granted by the Head of my Department or by his representatives. It is understood that copying or publication of this thesis for financial gain shall not be allowed without my written permission.

Department of Geophysics & Astronomy

The University of British Columbia
2075 Wesbrook Place
Vancouver, Canada
V6T 1W5

Date February 2, 1976

ABSTRACT

During July 1974, two reversed deep seismic sounding (DSS) profiles extending about 75 km were recorded in the Explorer Ridge region of the northeastern Pacific, one parallel and the other perpendicular to the ridge.

A two-ship operation was used to record near-vertical incidence to wide-angle reflected waves and refracted waves with penetration from the ocean bottom to the upper mantle. Signals from six individual hydrophones suspended at 45 m depth from a 600 m cable trailed behind the receiving ship were recorded in digital form. The shooting ship detonated charges ranging from 2.3 kg to 280 kg and recorded the direct arrival plus the WWVB time code.

Processing of the data recorded at distances beyond 4 km included demultiplexing, stacking, and filtering. Before the data were presented in record section form, traveltime corrections were made for topography and shot distance, and amplitude corrections were made for amplifier gain, charge size, and spherical spreading.

The interpretation procedure consisted of two steps. A homogeneous, layered velocity-depth model was initially constructed from first arrival traveltime data. The p-Δ curve corresponding to this model was then altered until an amplitude fit was obtained using synthetic

seismograms. Weichert-Herglotz integration of the resultant p-Δ curve produced the final velocity-depth model. This traveltime and amplitude interpretation required the introduction of velocity gradients into the model.

The profile run across the ridge showed no anomalous behaviour as the ridge was crossed; the profile on the Juan de Fuca plate, paralleling the ridge, exhibited traveltime branch offsets and delays. These have been interpreted as due to faulting with a vertical component of offset of about 5 km. The reversed upper mantle velocities are 7.8 and 7.3 km/s in directions perpendicular and parallel to the ridge. Anisotropy is proposed to explain these different velocities. Compared with crustal sections from other ridge areas, the data require a thick "layer 3" (up to 7 km) near the ridge crest. The total depth to the base of the oceanic crust varies between 10 and 12 km except in the faulted region. The results of this study favor the hypothesis that Explorer Ridge is presently an inactive spreading center.

TABLE OF CONTENTS

LIST OF TABLES

LIST OF FIGURES

ACKNOWLEDGMENTS

I would like to first of all express my appreciation to Dr. R.M. Clowes for his guidance and encouraging support throughout the project. I am also grateful to Dr. R.A. Wiggins for the use of his computer routine (HRGLTZ) and his helpful suggestions regarding the interpretation procedure.

Due to the nature of the project considerable assistance was required during the field operations. The time and assistance given by R. Clayton and E. Waddington on the shooting ship and J. Davies and B. Narod on the receiving ship is greatly appreciated. In addition, I would like to thank E. Waddington for the use of slides taken during the cruise. I am also indebted to C. West and R.D. Meldrum for their generous efforts concerned with the instrumentation and recording systems for the project.

I am pleased to acknowledge the use of the ships CFAV ENDEAVOUR and CFAV LAYMORE and the cooperation and assistance given by their officers and crews. The Fleet Diving Unit, Pacific Maritime Command, Esquimalt provided explosive experts and their assistance is gratefully acknowledged. The seismology division of the Earth Physics Branch provided the anti-submarine projectiles.

During part of this work, the author was supported by a Graduate Research Fellowship from the University of

British Columbia. Financial support for the project was provided by National Research Council equipment grant E3235 and operating grant A7707. Additional funds were contributed by Mobil Oil Canada Limited and Shell Canada Limited.

1. INTRODUCTION

1.1 Tectonic Significance of Explorer Ridge

Explorer Ridge is a broad northeast-trending topographic feature in the northeast Pacific located between 49° and 51° North latitude and 129° and 131° West longitude. It is considered part of a ridge-transform fault system which marks the western boundary of the Juan de Fuca plate (Fig. 1.1).

Atwater (1970) has concluded that the Juan de Fuca plate is a remnant of the Farallon plate (McKenzie and Morgan, 1969) which was underthrusting the American plate but broke up during mid-Tertiary time. Because of the complex interaction among the Pacific, Juan de Fuca, and American plates following the breakup, the present role of Explorer Ridge in the tectonic activity is not clearly understood. Is it, in fact, an active spreading center, offset by transform faults from other likely spreading centers as the inset in Fig. 1.1 suggests? While Juan de Fuca Ridge has generally been accepted as an active spreading center on the basis of flanking magnetic lineations (Vine and Wilson, 1965; Vine, 1966), the distribution of earthquake epicenters (Tobin and Sykes, 1968), and numerous geophysical and geological studies near the ridge (Dehlinger et al, 1970), no such conclusion can be reached for Explorer Ridge.

Figure 1.1 Location of deep seismic sounding profiles near Explorer Ridge. Solid circles show drift track of the receiving ship; heavy solid lines show track of shooting ship. Regions of normal magnetic polarity in the area of the survey are strippled. Bathymetric contours in meters (from Tiffin and Seeman, 1975). The inset shows the major tectonic features in the northeastern Pacific and outlines the map area given in detail.

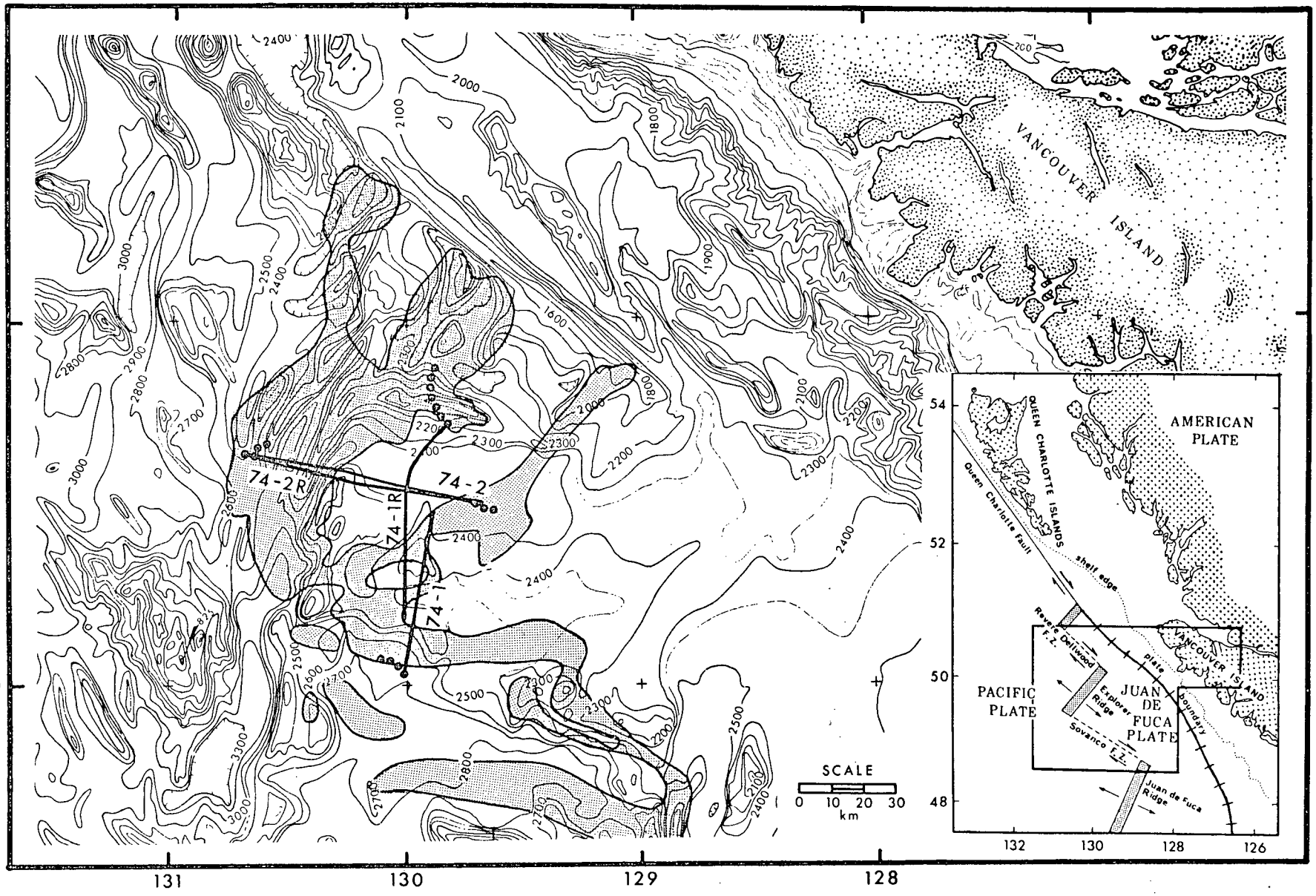
VANCOUVER ISLAND
74-2R
74-2
74-1R
74-1
SCALE
0 10 20 30
km
AMERICAN PLATE
QUEEN CHARLOTTE ISLANDS
Queen Charlotte Fault
shelf edge
Revere Dellwood F.Z.
Explorer Ridge
Sovanco F.Z.
Juan de Fuca Ridge
PACIFIC PLATE
JUAN DE FUCA PLATE
plate boundary
VANCOUVER ISLAND
50
49
131
130
129
128
54
52
50
48
132
130
128
126

Bertrand (1972) has presented evidence indicating that the Dellwood Knolls lying northwest of Explorer Ridge are part of a presently active spreading segment, He proposes that the eastern arm of Explorer Ridge (as delineated by the bifurcated central magnetic anomaly pattern in Fig. 1.1) ceased being active when the Dellwood segment came into existence (<1 m.y. ago). The possibility that Explorer Ridge is no longer active seems to tie in well with the earthquake data for Juan de Fuca plate. The epicenters given by Tobin and Sykes (1968) plus those compiled by Barr and Chase (1974) suggest that the Sovanco Fracture Zone is presently not an active transform fault. Rather, the Queen Charlotte Fault presently may extend to the northern tip of Juan de Fuca Ridge implying that Explorer Ridge no longer functions as an active spreading center (Barr and Chase, 1974). Such a change could be due to the reorientation of the Juan de Fuca Ridge which began about 7.5 m.y. ago according to magnetic anomaly patterns (Vine, 1966; Menard and Atwater, 1968). Explorer Ridge is then an offset segment of the Juan de Fuca Ridge (McManus et al, 1972) and the Dellwood Knolls are descendants of the Explorer segment (Bertrand, 1972).

From their study of ocean ridges and fracture zones off California, Menard and Atwater (1969) concluded that ". . . an entire section of a ridge may become inactive if it is too far from the general line of a ridge crest." If Explorer Ridge is now "too far" from Juan de Fuca Ridge, it may indeed be inactive. According to that reasoning the

Dellwood Knolls should also be inactive. However, Bertrand (1972) also considers the diffuse nature of the Queen Charlotte Fault Zone as an alternative explanation for the activity in the Dellwood area.

1.2 Previous Studies of Explorer Ridge

The bathymetric, magnetic, and earthquake data presently available have undoubtedly been valuable for inferring the possible status of Explorer Ridge in terms of the regional tectonics. However, few investigations have been attempted to determine the crustal/upper mantle structure near the ridge and then test the compatibility of this structure with the tectonic hypotheses. Except for a limited interpretation of gravity data from the area (Stacey, 1973), and the results of an in progress detailed study which includes continuous seismic profiling and dredge samples (A.G. Thomlinson, pers. comm., 1975), little information about the crustal structure near Explorer Ridge is known to exist.

1.3 Purpose and Scope of the Project

In order to obtain data for a detailed study of the crustal structure near Explorer Ridge, a deep seismic sounding (DSS) experiment was carried out during July, 1974. Using a two-ship operation, two reversed profiles about 75 km long were recorded - one parallel (on the Juan de Fuca plate), and the other perpendicular, to the ridge. Although seismic arrivals

ranging from near-vertical incidence reflections to wide-angle reflections and refractions were recorded, only data obtained beyond the critical distance for the first crustal layer (about 4 km) were completely processed and interpreted.

With these data, the purpose of this thesis project became twofold: (1) to obtain a velocity versus depth model for each profile through an interpretation based on seismic ray theory; (2) to consider the geological and tectonic implications of these models. The major emphasis of this thesis is on the first topic. The interpretation utilizes both traveltime and amplitude information, although a preliminary interpretation was made on the basis of first arrival times alone. Considerable attention was therefore given to processing the data in a manner which would facilitate this type of interpretation. Although determining what the velocity-depth models mean in terms of the geology and tectonics is probably the most rewarding part of such a study, it is also the most ambiguous. The chapter entitled "Discussion of Results" attempts to construct a geological model for the crust in the region covered by the profile lines. It was satisfying to note that several consistencies between the geological interpretation and present ideas regarding plate tectonics in the region did appear.

2. DATA ACQUISITION

2.1 The Two-Ship Operation

The two-ship operation used to record the four DSS profiles marked on Fig. 1.1 is similar, in principle, to the technique described by Shor (1963). A standard procedure involves using one of the ships for shooting and the other for receiving. During this project CFAV LAYMORE served as the shooting ship while CFAV ENDEAVOUR served as the receiving ship.

During a profile run ENDEAVOUR would drift freely from the starting point of the profile (indicated by dots in Fig. 1.1) while trailing a main cable which supported six individual hydrophone systems. Meanwhile LAYMORE would proceed along a predetermined course (solid track lines in Fig. 1.1) as charges were detonated at selected distances. Shot spacing was less than 0.5 km for the smallest charges (2.3 kg) where sub-critical reflections were anticipated, between 1 and 4 km for intermediate charges (4.5-45.4 kg), and around 5 km for the largest charges (94 and 282 kg) used beyond 45 km. Ship-to-ship distances were determined by radar out to about 22 km. Beyond that, Loran fixes were required to determine latitude and longitude from which distances could be calculated. To reverse the profile, ENDEAVOUR would steam to the final position of LAYMORE where shooting would begin in the

opposite direction.

Two such reversed profiles, one parallel and the other perpendicular to Explorer Ridge were planned and carried out. However as Fig. 1.1 shows, profiles 74-1 and 1R are not reversed well. Profile 74-1 was terminated at a distance of about 48 km due to sea conditions which prevented safe detonation of large charges. Navigation of LAYMORE relative to ENDEAVOUR and the large northwesterly drift of the latter ship for profile 74-1R caused the bow in the shooting track. In contrast, profiles 74-2 and 2R are well reversed.

The upper part of Fig 2.1 schematically shows the operational program. Details of the equipment and procedures are given in the following sections.

2.2 The Shooting Ship

SHOOTING PROCEDURES

Two types of explosives served as seismic energy sources during a profile run. For shot-receiver distances less than 45 km, 2.3 kg (5 lb) cartridges of Geogel[1], a gelatin explosive, were used to construct charge sizes up to 45.4 kg (100 lb). At longer distances, surplus Mark IV H.E. anti-submarine projectiles were used. These contained 94 kg (207 lb) of Minol high explosive. Detonating three projectiles simultaneously provided the maximum charge size

[1] Trademark of CIL explosives.

Figure 2.1 Top - The two-ship deep seismic sounding system with ray paths indicated for the direct water wave and some reflected and refracted waves. Bottom - A detailed view of one of the six hydrophone systems connected to the main cable.

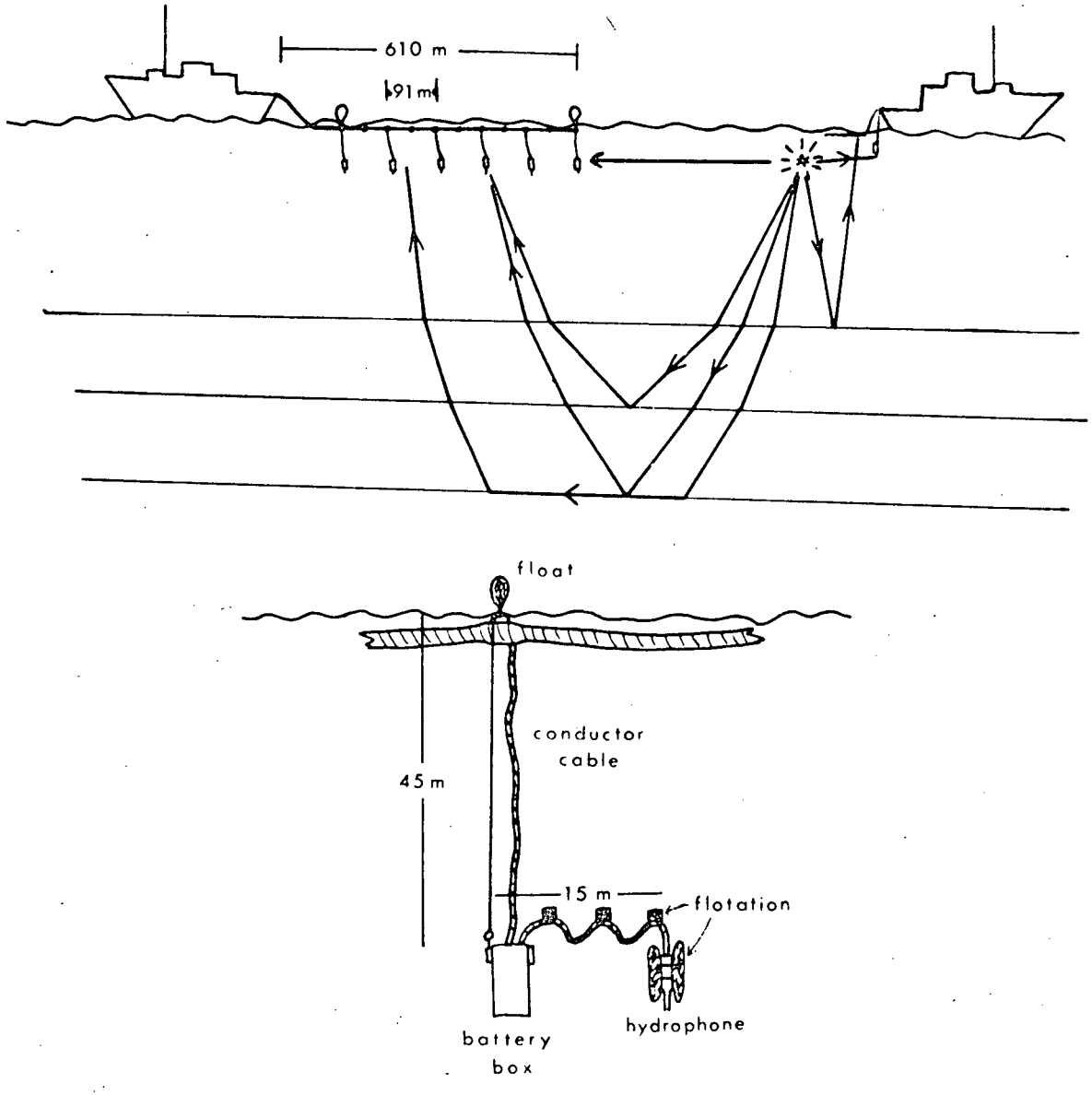
610 m
91 m
float
conductor
cable
45 m
15 m
flotation
hydrophone
battery
box

used, 282 kg (621 lb). Because the explosives used were so dissimilar in type and size, separate shooting techniques had to be employed.

Shooting procedures using Geogel were relatively simple and are essentially the same as those outlined by Shor (1963). Charges were prepared for detonation with a timed-fuse/Seismocap[2] assembly and Primacord[3]. After the charge was fastened to a 45 m line which had one or more balloons tied to the end of it, the fuse was lit and the charge was dropped overboard. A four minute fuse allowed time for the charge to sink to the optimum depth[4] (45 m). It also gave LAYMORE time to travel a safe distance ahead of the shot. After the shot had detonated, the range and bearing of the balloons were estimated and recorded.

Because the weight of the projectiles (170 kg including casing) made them unwieldy, a special procedure was used to detonate them safely. The timed-fuse/Seismocap assembly was connected to the Primacord and the fuse ignited

---

[2] Trademark of CIL explosives.

[3] Trademark of Ensign-Bickford Co., Simsbury, Conn.

[4] The criteria for optimum depth is that, for a given charge size, the detonation depth should equal a quarter of the wavelength for the bubble pulse frequency (Shor, 1963). Since charge size and detonation depth can be related to bubble pulse frequency by the Rayleigh-Willis formula (Kramer et al, 1968), a curve relating optimum charge depth or frequency to charge weight can be obtained. Such a curve is given by Raitt (1952) and was used to determine the 45m depth for the Geogel charges (60% dynamite). This depth represents an average for the range of Geogel charge sizes, and since the curve was calibrated for TNT, the true optimum depth may differ from this value by up to 15 m for a particular shot.

when the projectiles were a safe distance from the ship, rather than on board. To do this, a projectile or a group of three mounted on a pallet were suspended from a raft at a depth of 107 m[5] while LAYMORE moved about 2 km away. Using a motorized rubber boat, the Canadian Forces demolition team approached the raft, made the connections and radioed back to the ship when the fuse was ignited. The range and bearing of the shot were determined by the ship's radar.

A view of the shooting operations that have been described above is provided by the photographs in Fig. 2.2.

INSTRUMENTATION

Fig. 2.3 shows the instrument arrangement used on the shooting ship to record the direct arrival from the shot and the WWVB time code. The direct arrival was detected by a hydrophone trailed immediately behind the ship and a geophone placed on the deck. These signals, together with the time code were recorded on FM tape for subsequent playback. A two-channel chart recorder monitored the hydrophone and WWVB output. In addition to these instruments, a fathometer was used to obtain a continuous record of the water depth during the profile.

---

[5] Again, this depth (107 m) was considered optimum for the charge sizes involved. An expected consequence of the increased detonation depth is the increase in bubble pulse frequency. The change in frequency corresponding to the change from the Geogel to the projectiles can be observed on the seismic record sections and will be pointed out later.

CFAV LAYMORE

CFAV ENDEAVOUR

Figure 2.2A The shooting ship (CFAV LAYMORE) and receiving ship (CFAV ENDEAVOUR) used for the DSS project.

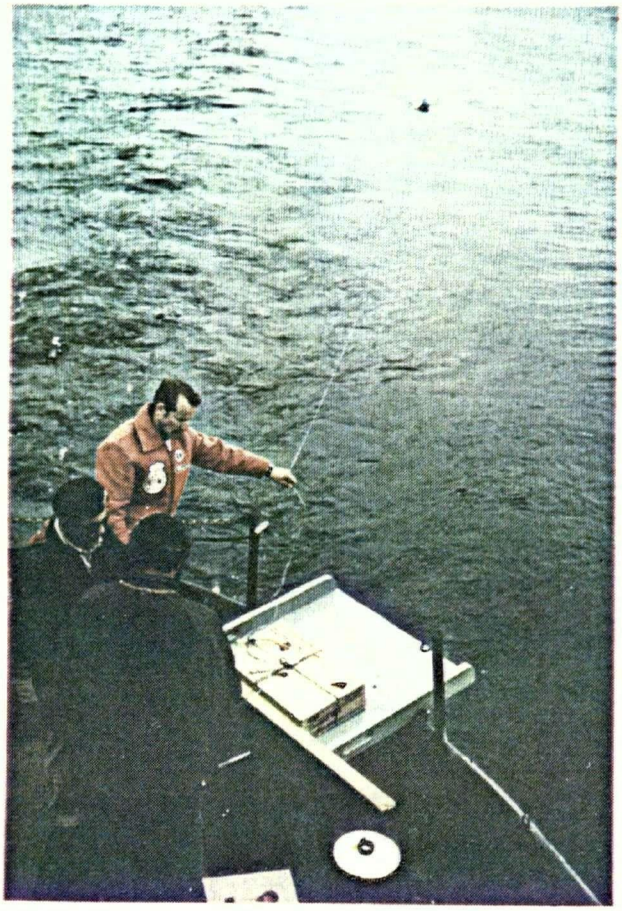

Figure 2.2B Shooting procedures with the gelatin explosives (Geogel). Top - A 11.2 kg (25 lb) charge is prepared for detonation. Bottom - a larger charge, 22.5 kg (50 lb) is ready to be dropped overboard with the tiltboard.

Figure 2.2C Top - Placing overboard the raft which supports the projectiles. Bottom - Towing the raft away from the ship as detonating cord is paid out from the zodiac.

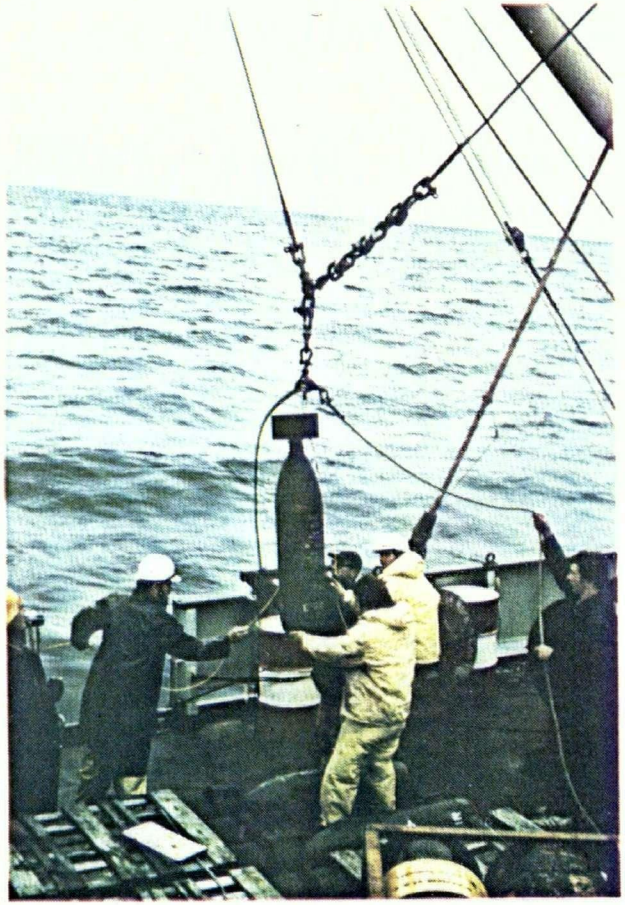

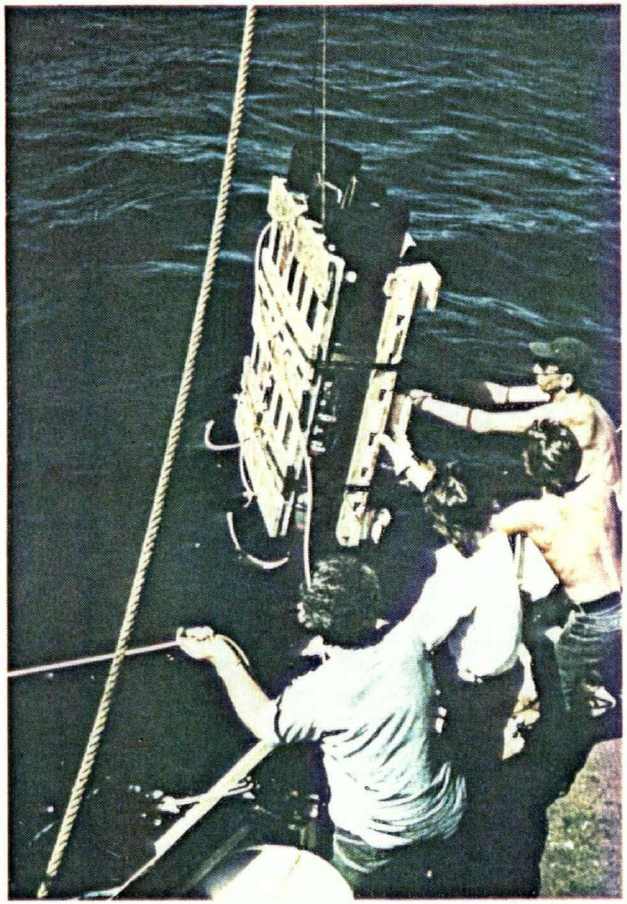

Figure 2.2D A single anti-submarine projectile (left) and a pallet of three (right) being lifted overboard.

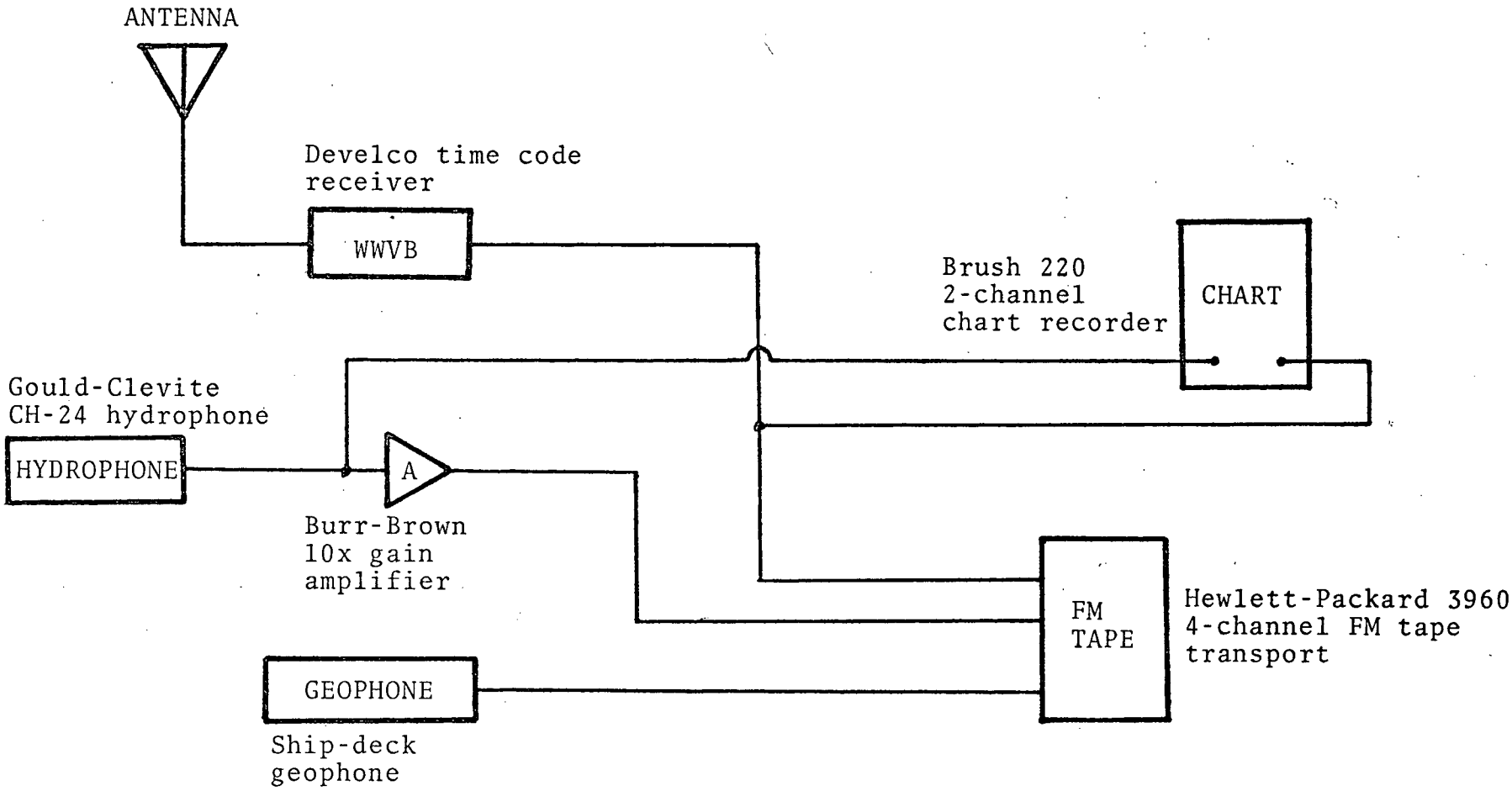

Figure 2.3 Block diagram of shooting ship instrumentation.

2.3 The Receiving Ship

RECEIVING PROCEDURES

Compared to shooting, the receiving operation required fewer manual tasks to run a profile. Before shooting began, the 610 m main cable was streamed from the stern and the six hydrophone systems were connected to takeouts spaced 91 m apart in a manner much as Fig. 2.1 (lower) shows. The procedure also involved performing a test for continuity between the hydrophone and recording equipment after each system had been placed overboard.

During a profile run the main cable was generally left to trail freely behind the ship. Shock cord extending from the main cable to the battery box, and a flexible 15 m cable which led to the hydrophone systems, provided mechanical damping to minimize the effects of surface waves. At some of the greater distances however, where high signal-to-noise ratios were more difficult to achieve, additional methods were employed to minimize these effects. First of all, maneuvering ENDEAVOUR to place the main cable in a "U" configuration improved the data as the tension on the cable was reduced. In conjunction with this, a tensioning/slackening procedure was also carried out at larger distances. By maintaining tension on the cable with a windlass, and then rapidly releasing it just before the shot, the hydrophones were slowly drifting downward when the seismic arrivals were detected. Although such techniques involved an extra effort for each shot, the improvement in the quality of the data was significant as

noise levels were observed to decrease by factors of at least two or three.

INSTRUMENTATION

The recording system used on the receiving ship is shown in Fig. 2.4. Pressure waves incident on piezoelectric crystals produce a signal which is preamplified (20 db) and transmitted to the seismic amplifiers on board. In the latter, the signal is bandpass filtered between 0.8 and 100.0 hz, then amplified with the gain manually set for each shot. The outputs from the six seismic amplifiers plus the WWVB time code are recorded on magnetic tape with an IBM-compatible, 14 bit, multichannel digital acquisition system. As a backup, the data also were recorded in analog form on a seven channel FM tape recorder. If the digital system had failed, the FM tapes could have been digitized at a later time. Five data channels and the WWVB signal are monitored on a six-channel chart recorder. This enabled quality control of the seismic data since required changes in charge size could be relayed to the shooting ship via two-way radio. A fathometer on the receiving ship provided a record of the seafloor topography as the ship drifted.

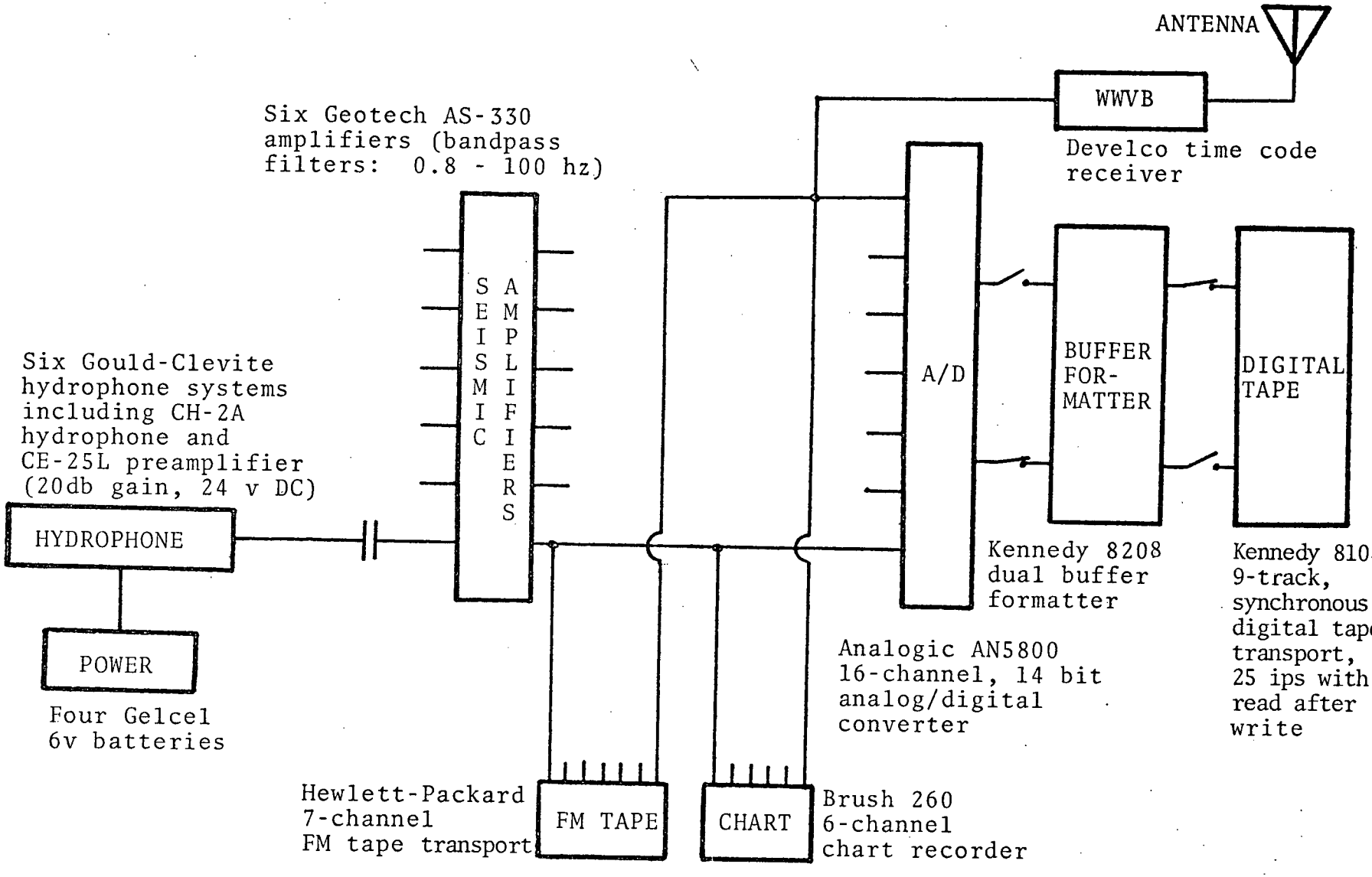

Figure 2.4 Block diagram of receiving ship instrumentation.

3. DATA PROCESSING

A description is given here of the procedure followed to process the seismic data and present them in record section form. By making appropriate traveltime and amplitude corrections the final record section can be reliably interpreted using synthetic seismograms.

3.1 Field Tapes

Following the cruise, the magnetic tapes recorded on board the receiving ship were checked to ensure that the digital system had functioned properly. However the data were in an impractical form to access for routine processing. The multichannel data had been multiplexed which meant that reconstructing the data for each channel would be time-consuming from the computing standpoint. Also, the digital system writes the data in an unblocked format (each logical record is one block) which is inefficient for tape input/output (I/O) operations. In addition, the amount of data recorded was excessive. Normally digitization lasted for about a minute for each shot in order to acquire a complete time code. However, useful seismic data may have been recorded during less than half of this interval. Finally, the recording density was 800 bytes per inch (BPI) rather than the more standard

1600 BPI. This meant the amount of tape used was inherently larger than necessary.

For the above reasons, and others as well, the raw data were edited, demultiplexed, and written on new tapes in a blocked format at the higher recording density. The IBM 370/68 computer which operates under the Michigan Terminal System (MTS) at the University of British Columbia was used for these and all further digital processing operations.

3.2 Shot-Receiver Distances

Shot-receiver distances for each shot were calculated using direct water wave (DWW) traveltimes and a constant for the DWW velocity. A seven-channel computer plot of digital data was used to determine DWW arrival times relative to UT within 0.01s. The origin time of the shot relative to UT was obtained from an FM playback of the single hydrophone and WWVB signals onto a two-channel chart recorder. Although the shot could be timed to better than 0.005s on the chart record, an additional error of up to 0.015s was introduced when the correction for the estimated shot-to-ship distance was considered.

A DWW velocity of 1.48 km/s (Minkley et al, 1970) was assumed to convert traveltimes to distances. Although this value does change with depth and season, the variation is less than one per cent. Taking into account the error associated with DWW traveltimes and the DWW velocity, the error

in distance calculations was less than three per cent.

3.3 Traveltime Corrections

Errors in seismic traveltimes are primarily due to inaccurate origin times and topography. Corrections for these errors are discussed below.

ORIGIN TIMES

The distance between the shot and the hydrophone behind the shooting ship introduces a time delay before the shot is recorded. As a result, the observed seismic traveltimes will be less than they actually are. The correction for the delay time is calculated from the estimated shot-hydrophone distance and DWW velocity of 1.48 km/s. For small charges using Geogel, the shot distances were estimated according to the location of the surface balloons after the shot. Distance estimates ranged from 90 to 275 m, or in terms of origin time corrections, from 0.061s to 0.186s. For the large charges where radar was used, distances ranged form 0.5 to 1.8 km; corresponding time corrections were between 0.337 and 1.216s.

It is also important to consider the error associated with the origin time corrections, particularly since some of the distance estimates were very subjective. Although the distance to the balloons was never measured and compared with estimates, an attempt was made to calculate it. Some timely photographs provided slides showing the balloons immediately after the shot. From the slides, the size of the balloons'

image produced by the camera lens could be determined. Since the object size and image distance (focal length of the lens) were known, the object distance could be calculated using geometrical optics. The results compare favorably with the estimates; the difference was less than 10 m in each of the three shots considered.

Based on the accuracy of the measurements used in the distance calculation, a maximum error of seven per cent was assigned to the distance estimates. Assuming a maximum one per cent error in the DWW velocity, the error in the origin time correction for the small charges is 8 per cent, or up to 0.015s. The error in distances determined by radar was much smaller, around two percent or less. Therefore, a maximum error of 0.015s is also considered appropriate for the large charges.

TOPOGRAPHY

Traveltimes also were corrected for seafloor topography as recorded on both the shooting and receiving ships. A water depth datum of 2.40 km was chosen because it minimized the magnitude of the corrections. The bathymetry records from the receiving ship showed little variation throughout any profile except 74-1R where considerable drift occurred. Recorded water depths on the shooting ship ranged from 2000 m to 2600 m in the ridge areas but were generally within 75 m of the datum level on the flanks.

To calculate the topographic correction at either the shot or receiver location, the following expression was used:

$$\Delta t = (D - d_r) \frac{(V_\ell - V_W)}{V_\ell V_W}$$

where D is the datum depth, d_r is the recorded depth, V_ℓ is the velocity of the uppermost layer, and V_W is the DWW velocity. For all calculations, values of 3.0 km/s and 1.48 km/s were assumed for V_ℓ and V_W, respectively. The traveltime must be increased ($\Delta t > 0$) to compensate for the hills and decreased ($\Delta t < 0$) to compensate for the valleys in the topography.

The net topographic correction for each shot is simply the algebraic sum of the shot and receiver corrections. The magnitude of the net correction was generally less than 0.035s except in areas showing large topographic relief. Here, corrections up to 0.220s were calculated.

The error in Δt was difficult to evaluate since the accuracy of values for V_ℓ and d_r are not well determined. However, an error estimate of 0.25 km/s in V_ℓ based on the range in velocities that has been associated with the sedimentary/basement layer, and an error of 0.005 km in d_r associated with reading the bathymetric record, yields a total error of 16% in Δt. This amounts to 0.005s or less for locations having small topographic corrections.

3.4 Amplitude Corrections

In order to facilitate an amplitude interpretation of the data, corrections were made for variations in amplifier settings, charge size, and shot-receiver distance. A simple computer routine was used to calculate these corrections for

the six channels of every shot and also return a normalized set of correction factors for the entire profile.

AMPLIFIERS

Manual gain control on the seismic amplifiers allowed near shots to be attenuated and distant shots to be amplified relative to the first stage of amplification of 70 db. In order to develop an expression for the necessary correction factors, the following definition is first considered:

$$\text{Voltage gain (db)} = 20 \log_{10} \frac{V_2}{V_1}$$

where V_1 and V_2 are two voltage levels of the signal. Since absolute voltage values are not relevant here, the expression can be simplified by assuming an instantaneous value of 1v for the signal after being initially amplified by 70 db. If the signal has been amplified by an additional G db so that $G = 20 \log_{10} V_2$, then multiplying the recorded signal by $1/V_2$ will bring it back to its original value, i.e. 1v. The correction factor, $1/V_2$, denoted as C_1 is then, $C_1 = 1/V_2 = 10^{-G/20}$. Note that if the input signal has been attenuated ($G < 0$) rather than amplified, the exponent is positive. Multiplying by C_1 will then increase the amplitude of the recorded signal.

CHARGE SIZE

Based on studies of underwater explosions, O'Brien (1960) has shown that first arrival seismic amplitudes are proportional to $W^{\frac{2}{3}}$ where W is the weight of the charge. Later experimental work by Muller et al (1962) also placed the value of the exponent close to two thirds. The amplitude correction for

charge size, denoted as C_2, is $C_2 = 1/W^{\frac{2}{3}}$ where W is given in lbs.

This correction was applied to all shots in each profile. However, since two types of explosives were used and were detonated at different depths, they are not equivalent in terms of energy yield per pound. No attempt was made to correct for this. The difference may therefore cause some peculiar amplitude (and frequency) changes to appear on the record section.

SPHERICAL SPREADING

A correction must also be made for the decrease in amplitude as seismic energy spreads away from the shot. Červený and Ravindra (1971, p. 147) show that for large epicentral distances (r), the head wave amplitudes decrease approximately as $1/r^2$ with increasing r. For small r, near the critical distance, the rate may be closer to $1/r^3$ or $1/r^4$. Wide-angle reflections, on the other hand, have amplitudes which fall off as 1/r with increasing r. (Braile and Smith, 1975). Although it was not completely suitable, the correction factor $C_3 = r^2$ was applied to all data.

THE NORMALIZED CORRECTION FACTOR

The amplitude correction (C) applied to a given data channel can now be written as

$$C = \frac{C'}{C'_{max}} \quad \text{where } C' = C_1 \cdot C_2 \cdot C_3 = 10^{-G/20} \cdot W^{\frac{-2}{3}} \cdot r^2$$

and C'_{max} is the maximum product calculated. C'_{max} is used to normalize values of C to lie between zero and one.

3.5 Seismic Record Sections

The raw data from each profile were initially presented in record section form by plotting all six channels of demultiplexed data for each shot. Corrections were made for traveltimes but not amplitudes. For plotting, traveltimes were reduced by x/6s where x is the shot-receiver distance.

Fig. 3.1 shows the raw data from profile 74-2 beginning at a distance of about 4.5 km. Far more data is presented here than will be interpreted later. However, the intent was to show later phases such as bottom reflections and multiples, and also to present a better view of the overall quality of the data.

STACKING

The next step involved stacking the six seismograms to form a single trace for each shot. The primary reason for stacking was to enhance the quality of the data. At the same time it reduced the amount of data to be handled and, therefore cut computing and plotting costs.

In general, to stack multichannel data, the summation is performed along some predetermined lag trajectory. As the title implies, the lag trajectory is defined by the lag, or equivalently, the moveout of a signal from one channel to the next due to receiver spacing. For reflection arrivals, the trajectory is hyperbolic. If, however, we assume the trajectory is a straight line for refraction arrivals, the

Figure 3.1 Record section of six channel data from profile 74-2 recorded beyond the critical distance for the first crustal layer. Traveltimes have been corrected for topography and shot distance, but no amplitude corrections have been applied.

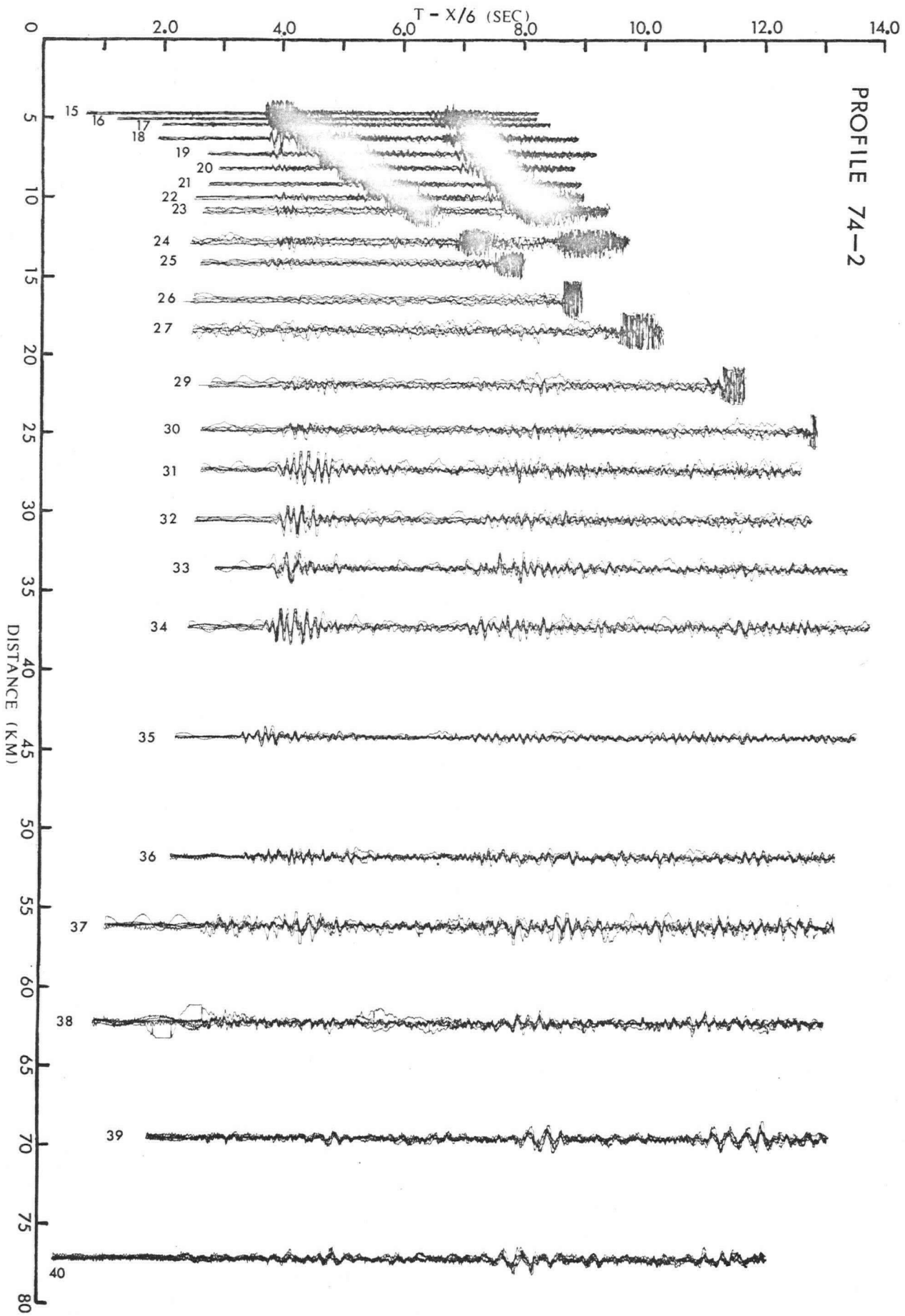
T - X/6 (SEC)
0
2.0
4.0
6.0
8.0
10.0
12.0
14.0
PROFILE 74-2
DISTANCE (KM)
5
10
15
20
25
30
35
40
45
50
55
60
65
70
75
80
15
16
17
18
19
20
21
22
23
24
25
26
27
29
30
31
32
33
34
35
36
37
38
39
40

stacking velocity will be the velocity of the critically refracting layer. More sophisticated techniques of determining the optimum stacking velocity employ coherency measures which test a range of velocities. Coherency measures were not applied however, since the number of data channels was considered inadequate for reliable results. Also, the spatial digitization was such that the velocity resolution would be no better than 16 km/s. Therefore, refraction velocities determined from the interpretation of first arrival traveltime data were used instead. For a particular shot, the optimum stacking velocity for the first arrival was used to obtain the entire stacked trace. This choice was made only after the effects of using different velocities to obtain later segments of the trace were shown to be insignificant.

The data from profile 74-2 after amplitude corrections and stacking were applied are shown in Fig. 3.2. Note that most of the large amplitude bottom reflections and their multiples have been omitted. The improvement in the data is quite striking, particularly for those shots recorded beyond 55 km where the signal/noise ratio was very low.

FILTERING

Although the amplifier filters provided filtering between 0.8 and 100.0 hz, some high frequency noise remained superimposed on the stacked traces. Also, the effect of the low frequency swell of the sea was still apparent on some traces. Therefore, the stacked data for each profile were bandpass filtered between 2.0 and 30.0 hz with a zero phase shift,

Figure 3.2 Record section of data from profile 74-2 after stacking to form a single trace for each shot. Both traveltime and amplitude corrections have been applied.

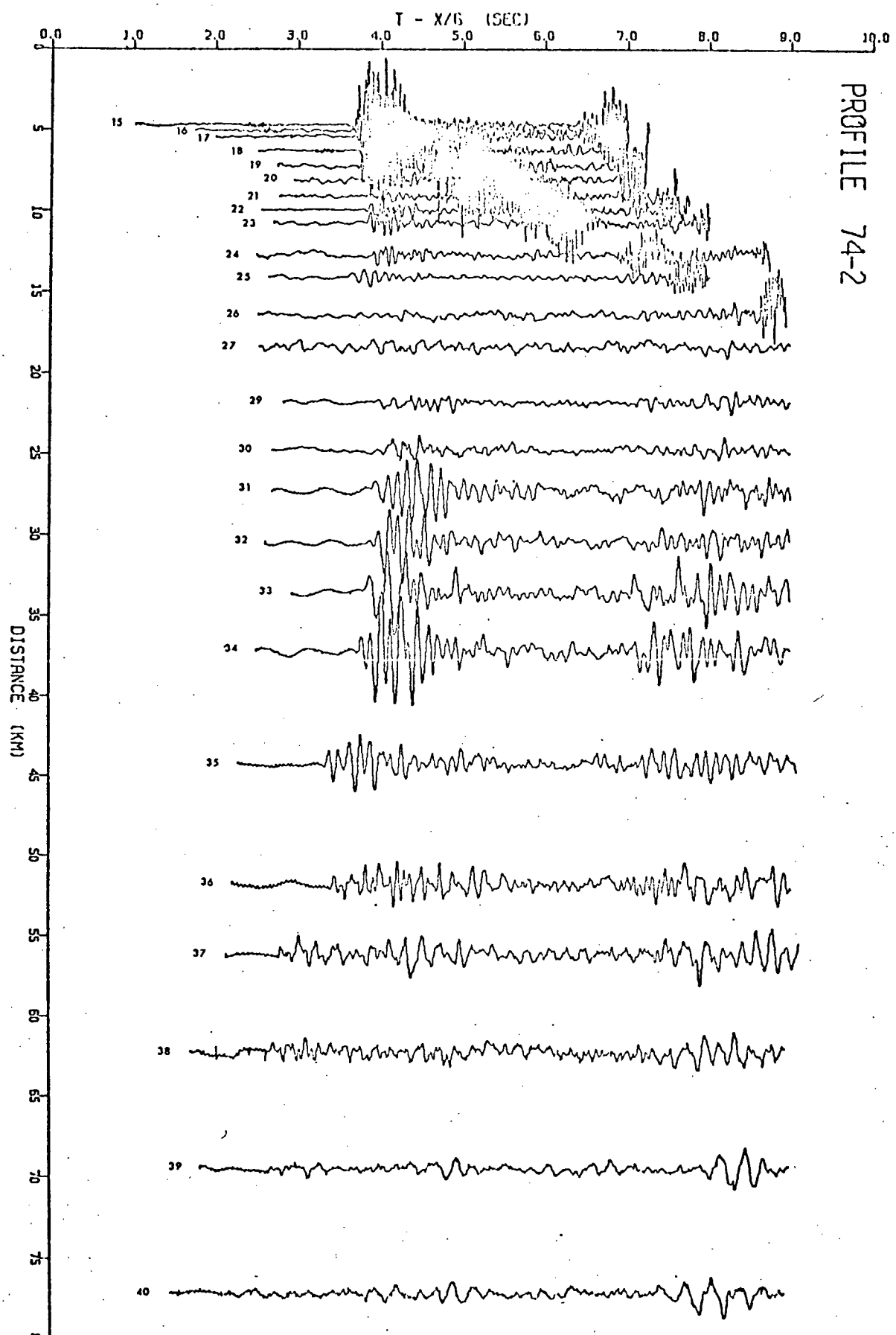
T - X/6 (SEC)
0.0
1.0
2.0
3.0
4.0
5.0
6.0
7.0
8.0
9.0
10.0
DISTANCE (KM)
0
5
10
15
20
25
30
35
40
45
50
55
60
65
70
75
80
15
16
17
18
19
20
21
22
23
24
25
26
27
29
30
31
32
33
34
35
36
37
38
39
40
PROFILE 74-2

fourth order, Butterworth filter. The mathematical background for Butterworth filters is given by Kanasewich (1973).

The frequency bandwidth was determined by measuring the period of prominent arrivals on the stacked traces; most values ranged between 8 and 12 hz. Such an approach was adequate since the purpose of bandpass filtering was simply to improve the general appearance of the data. In fact, the interpretation could have been accomplished equally well without any filtering.

After applying the amplitude corrections, stacking, and filtering, the processed version of the data for each profile was written on another tape. No data beyond 9.0s reduced traveltime were stored however. The processed data for the four profiles are presented in Figs. 3.3 through 3.6.

Figure 3.3 Record section of data from profile 74-1 after processing which included stacking, bandpass filtering (Butterworth, 2.0 to 30.0 hz) and applying traveltime and amplitude corrections.

PROFILE 74-1
T - X/6 (SEC)
DISTANCE (KM)
0.0
1.0
2.0
3.0
4.0
5.0
6.0
7.0
8.0
9.0
10.0
0
5
10
15
20
25
30
35
40
45
50
14
15
16
17
18
19
20
21
22
23
24
25
26
27
28
29
30
31
32
33
34
35
36
37

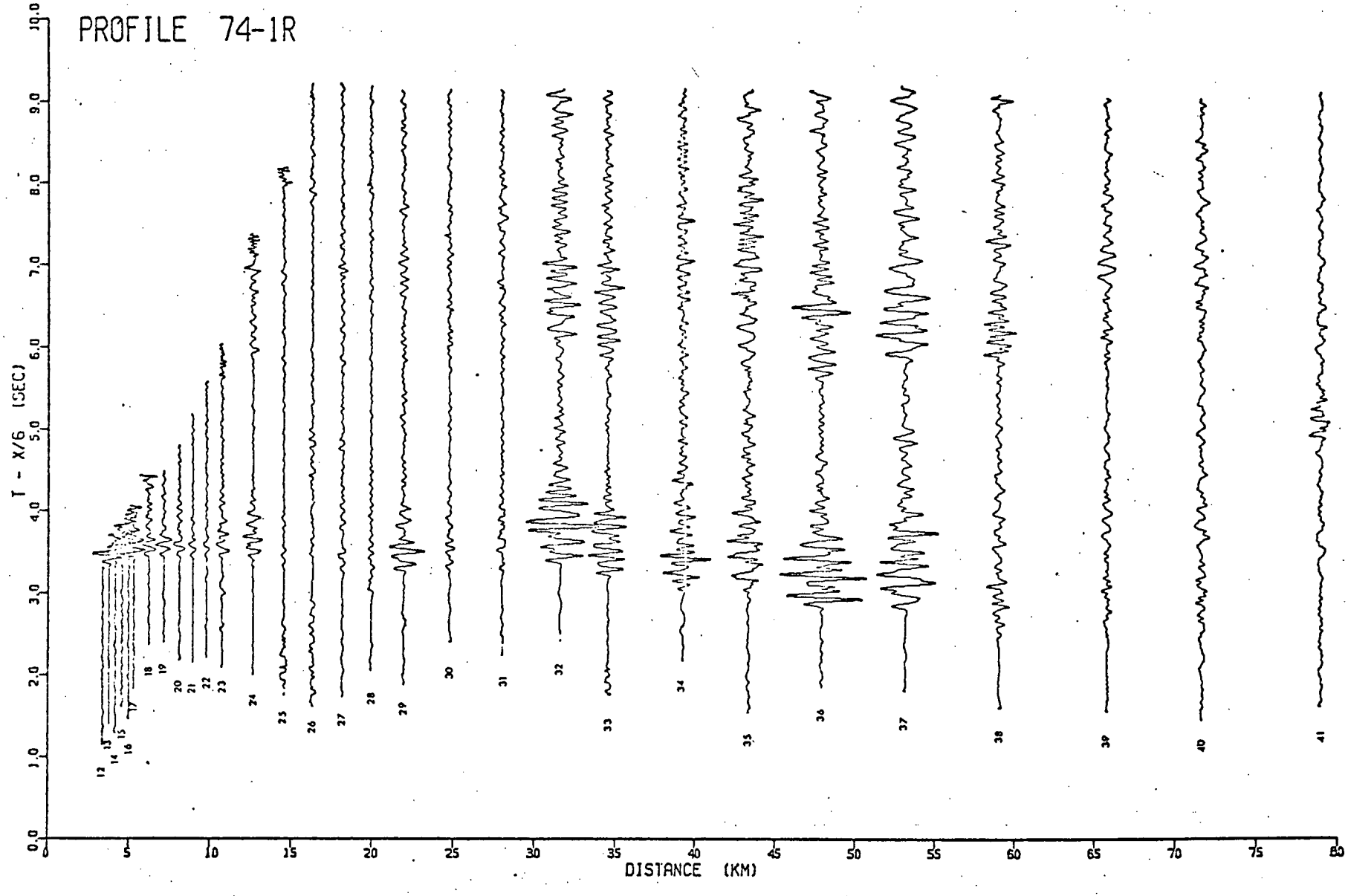

Figure 3.4 Processed record section for profile 74-1R.

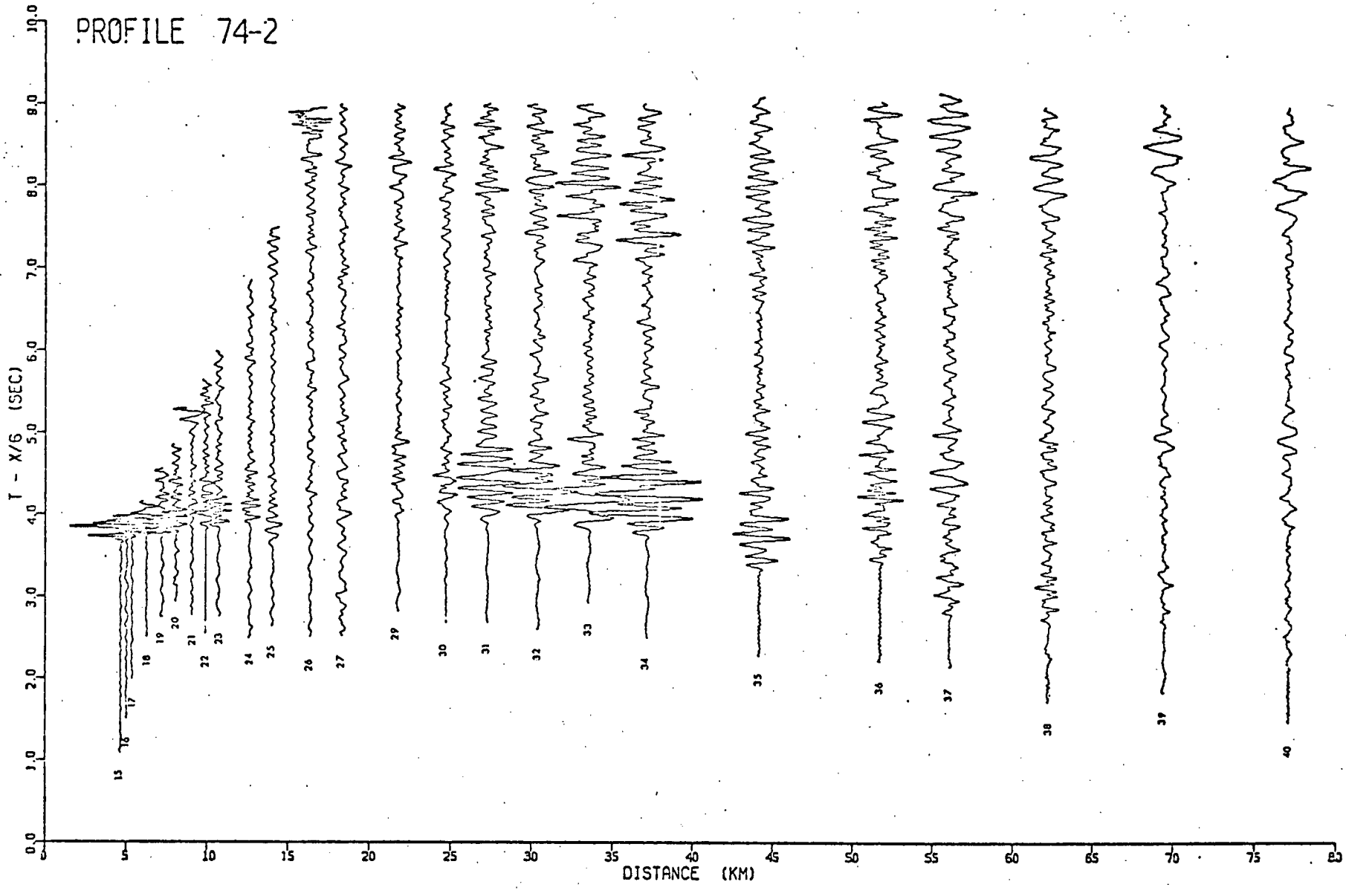

Figure 3.5 Processed record section for profile 74-2.

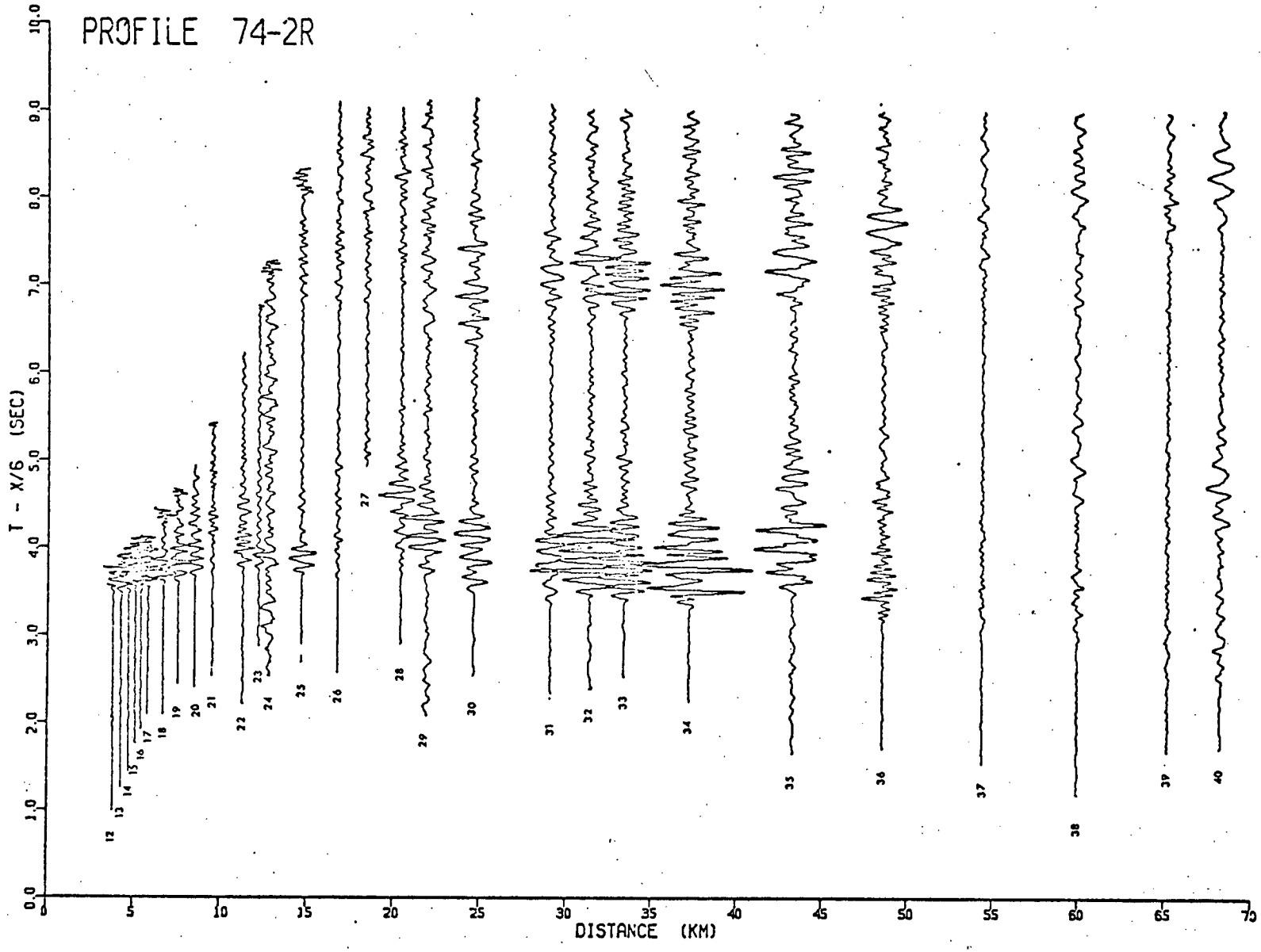

Figure 3.6 Processed record section for profile 74-2R

4. INTERPRETATION

4.1 Review of Methods

The interpretation of marine refraction data in the past has generally relied on the slope-intercept method to calculate velocities and depths from a plot of traveltime versus distance. The method was originally proposed for application to marine data by DeGoyler (1932). Since then, it has been widely used to interpret large quantities of data from deep ocean areas. While the method is simple to apply, two restrictive assumptions are made - that each layer is bounded above and below by planes and has a constant velocity which is higher than the one in the layer above it. In reality, of course, these conditions are not perfectly satisfied, and the resulting velocity-depth model may be highly artificial.

A more complete interpretation of the data can be made by utilizing both traveltimes and amplitudes. This method of interpreting marine refraction data has been demonstrated by Helmberger (1968), and Helmberger and Morris (1969, 1970) through the use of synthetic seismograms. A similar method is used in this work. It consists of obtaining first a simple layered model using the slope-intercept method on first arrival traveltimes; then using this model as a starting point, changes are made to it until the synthetic

seismograms match the amplitude characteristics of the data without disturbing the original traveltime fit. The details of this approach are given below.

4.2 Traveltime Interpretation

TRAVELTIME PLOTS

The traveltime plots used to derive the initial velocity-depth models were constructed from first arrival picks made on computer plotted seismograms. Fig. 4.1 shows four sets of such seismograms from profile 74-1R that were plotted at approximately 100 mm/s. Each set is characteristic of the data recorded on other profiles at distances similar to those indicated.

The first refracted arrival was readily identified on nearly all records. However, locating its first break was sometimes rather subjective especially at longer distances where the onset was more emergent and the background noise level was higher. Also, at a distance of about 12 km the direct wave and the seismic arrival interfered with one another causing the onset to be distorted for a few shots. The maximum error in timing the first arrival picks was determined to be 0.015s. Therefore, together with the error associated with the origin time and topographic corrections, the estimated traveltime error was less than 0.035s.

Figs. 4.2 and 4.3 are reduced traveltime plots of the first arrival data from the four profiles; the least squares fitted traveltime branches also are shown. In the lower

Figure 4.1 Computer plotted seismograms from four shots at different distances along profile 74-1R. One hydrophone system was inoperative for three of the four shots shown.

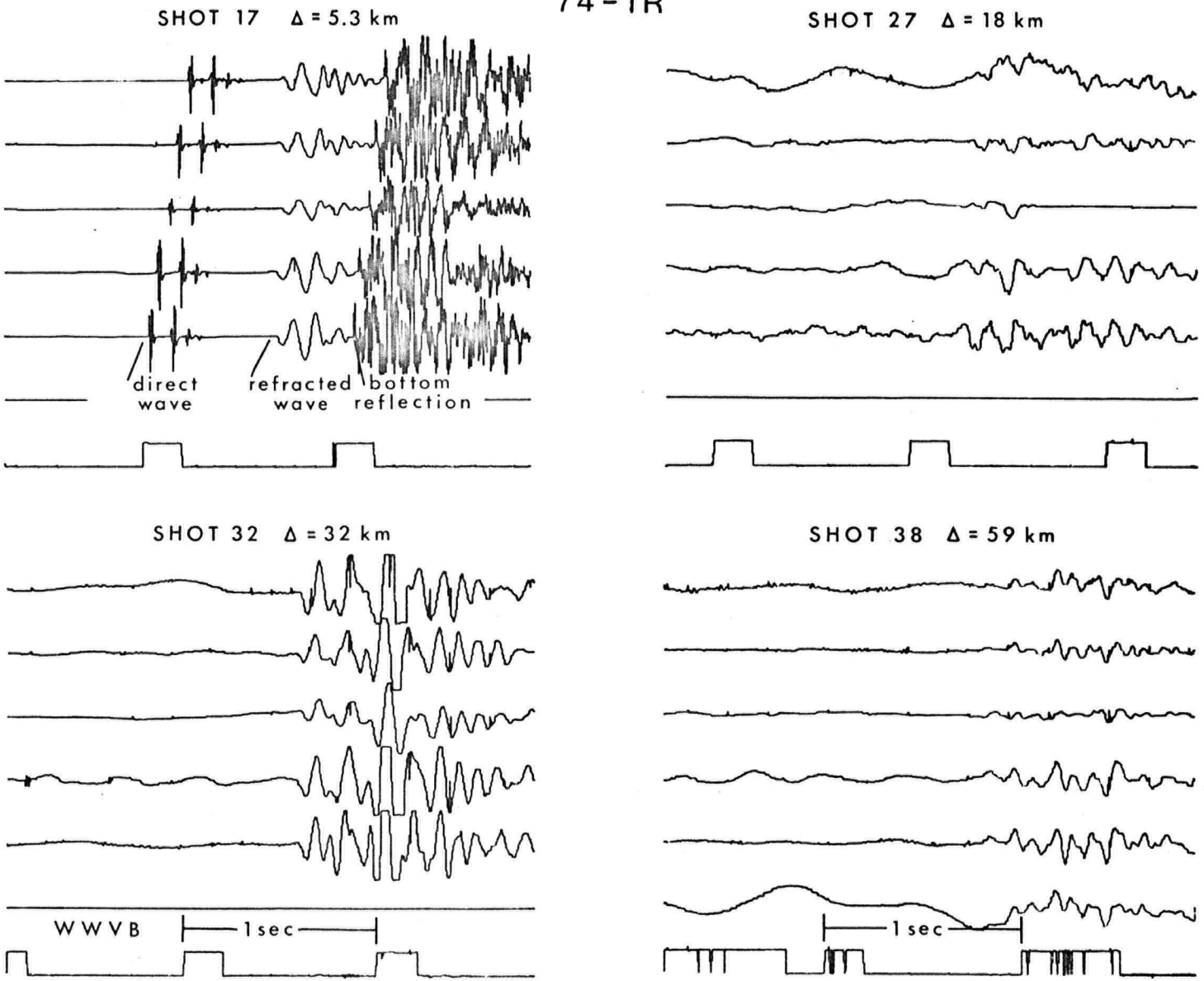
SHOT 17 Δ = 5.3 km
direct wave
refracted wave
bottom reflection
SHOT 27 Δ = 18 km
SHOT 32 Δ = 32 km
WWVB
1 sec
SHOT 38 Δ = 59 km
1 sec

Figure 4.2 Reduced traveltime data (symbols) and least squares fits (lines) for profiles 74-1 and 74-1R. The inverse slopes of the lines are velocities in km/s; intercepts are in sec. The upper part is an expanded scale to show the first 20 km of each profile. Symbols enclosed in parentheses were assigned a relative weight of 0.5.

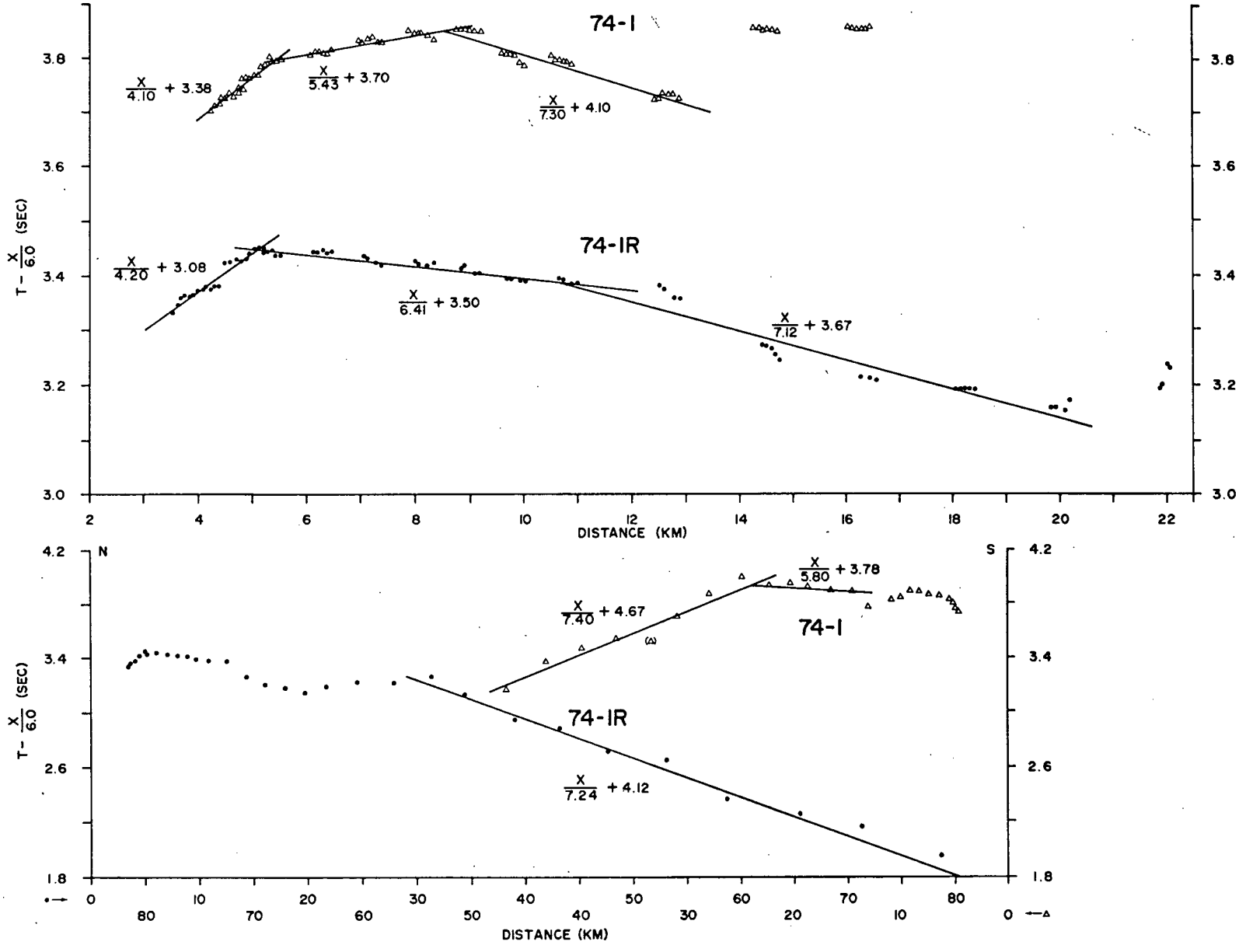
74-1
X/4.10 + 3.38
X/5.43 + 3.70
X/7.30 + 4.10
74-IR
X/4.20 + 3.08
X/6.41 + 3.50
X/7.12 + 3.67
T - X/6.0 (SEC)
DISTANCE (KM)
N
S
X/5.80 + 3.78
X/7.40 + 4.67
74-1
74-IR
X/7.24 + 4.12
T - X/6.0 (SEC)
DISTANCE (KM)

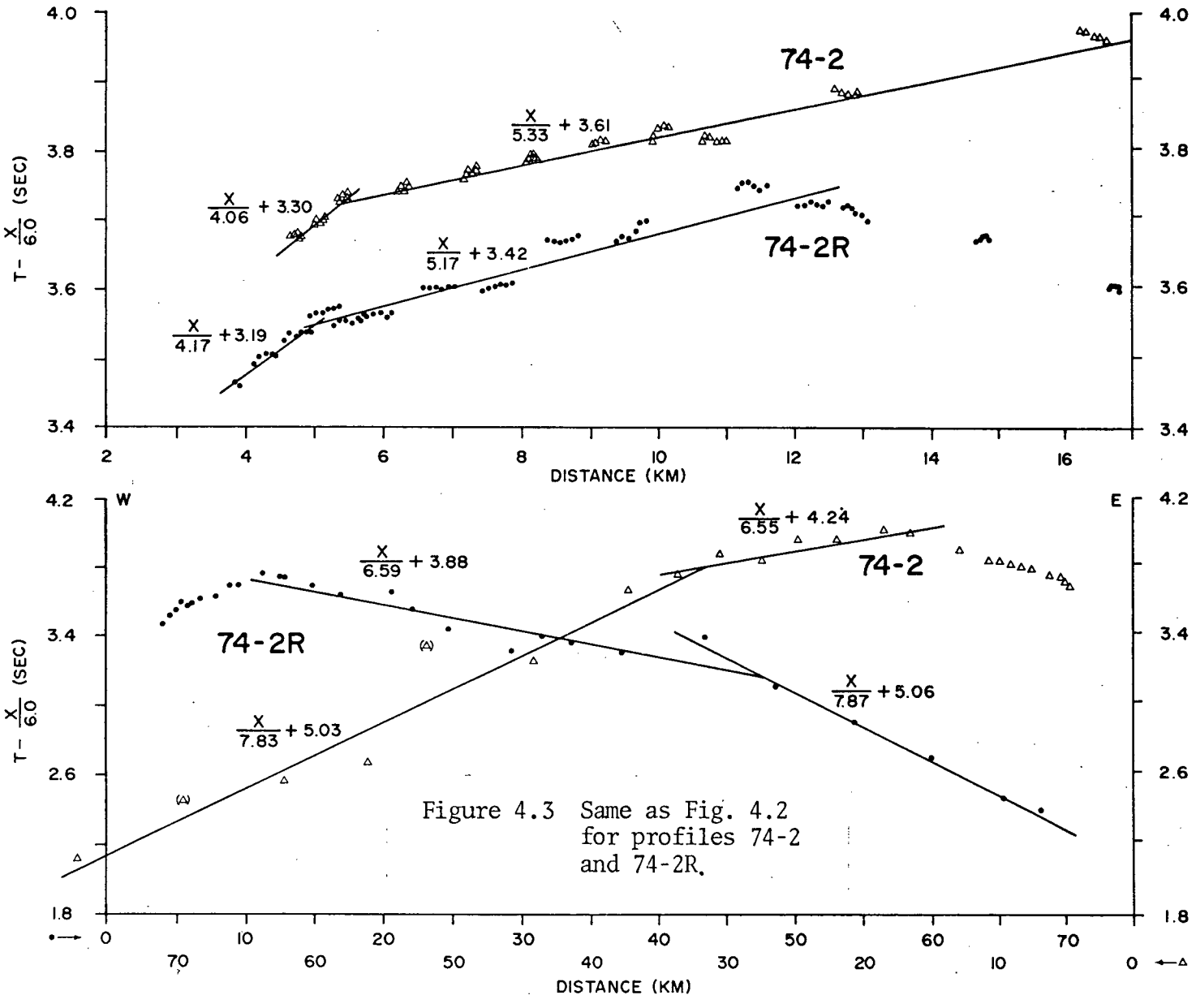

Figure 4.3 Same as Fig. 4.2 for profiles 74-2 and 74-2R.

part of each diagram a single data point is plotted for each shot although all the traces were generally used to make the pick. For the traveltime branches at the beginning of each profile, the number of points available for a least squares analysis was considered inadequate. The upper part of each diagram therefore shows, on an expanded scale, traveltimes determined from each seismic trace recorded over the first 20 km. Since the first arrival data over this portion of the profiles are not reversed, the upper plots both have the same origin.

A least squares linear fit was made and a velocity-depth model computed from slopes and intercepts. In addition to the data points, input to the computer program included a weighting value between zero and one for each point according to its estimated reliability. Deciding on which points to assign to each traveltime branch was a matter of judgement. In some cases, data points near a branch crossover position were assigned to each branch for the least squares analysis. As Figs 4.2 and 4.3 indicate, profiles 74-2 and 2R display normal traveltime curves (layer velocities increase with depth) while profiles 74-1 and 1R show anomalous behavior. The anomalies are too large to attribute to timing errors and so must be considered a real feature to be explained.

Let us examine in more detail the traveltime curves for profiles 74-1 and 1R that are shown in Fig. 4.2. Following the first branch there are intermediate branches with apparent velocities of 5.43 km/s (74-1) and 6.41 km/s (74-1R). These persist as first arrivals for a short distance after which a

branch with a higher velocity (7.30 km/s and 7.12 km/s for 74-1 and 1R, respectively) is observed. However this branch extends only for a few km on 74-1 and for about 10 km on 74-1R. At greater distances the first arrivals line up on branches with similar velocities, 7.37 km/s for 74-1 and 7.24 km/s for 74-1R but showing a clear time delay. The similarity of these apparent velocities which are partially reversed suggests that dip on the refracting horizon is negligible. In addition there exists an intermediate branch on 74-1 which has an apparent velocity of 5.80 km/s, a value near the average for the two intermediate branches at shorter distances.

How are such observations explained in a reasonable manner? A low velocity zone will introduce a time delay and offset into the first arrival traveltime curve. But if this were the case, data from 74-2 should exhibit a similar effect. They do not. Also a low velocity layer does not explain the intermediate 5.80 km/s branch.

FAULTING

An alternative explanation for the observations is a fault with a major component of vertical shift either due to downthrow in the direction of the traverse or equivalently, uplift in the region near the start of the profile. If the horizontal layers are terminated by a fault-like structure with a vertical offset in the order of a few kilometers, the seismic waves will be diffracted and scattered. Sufficient energy may then be incident upon the down-faulted block to create another head wave. For profile 74-1R the first arrival data at distances of 20 and 22 km (Fig 4.2 upper) clearly show a trend

characteristic of diffractions that would occur near a fault. In addition, the amplitude of the seismic trace at 22 km (shot 29, Fig. 3.4) is inconsistent with the amplitudes of adjacent records and may be attributed to a focusing effect associated with the fault. No such evidence is apparent for profile 74-1. For this profile however, the offset may be such that for a short distance first arrivals are from an unfaulted layer with apparent velocity 5.80 km/s before these waves are overtaken by arrivals from the material with velocity 7.40 km/s.

VELOCITY-DEPTH MODELS

Except for the faulted region of profile 74-1 and 1R, the velocity-depth structures for the four profiles can be obtained using two familiar expressions from refraction seismology; namely,

$$\frac{1}{V_n} = \left(\frac{dt}{dx}\right)_n \quad \text{and} \quad Ti_n = \sum_{j=1}^{n-1} 2z_j \frac{(V_n^2 - V_j^2)^{\frac{1}{2}}}{V_j V_n}$$

where $(dt/dx)_n$ and T_{i_n} are the slope and intercept, respectively of the traveltime branch for the n^{th} layer. V_n is the apparent velocity of the n^{th} layer and z_{n-1} is the thickness of the layer above it. Table I summarizes the results of the computations for each profile.

Using the velocities and intercepts, and assuming homogeneous layers, fault throws could be calculated according to the method outlined in the Appendix. The fault throws for profiles 74-1 and 1R are 3.9 and 4.7 km, respectively. The data given in Table 1 for each profile and the calculated fault structures for profiles 74-1 and 1R are presented graphically

Table I Summary of least squares analysis of traveltime data. Traveltime branches are numbered from near to far distances. One standard deviation in the determination of the slopes has been converted to an equivalent standard deviation in velocity. The calculated standard deviation in the intercept is given. Maximum residuals enclosed by parantheses are for points assigned a weighting factor of 0.5.

Profile	Figure Reference	Traveltime Branch	No. Pts.	Velocity (km/s)	Intercept (s)	Layer Thickness (km)	Maximum Residual (s)
74-1				1.48 (assumed)		2.68	
	3-upper	1	21	4.10 ± .06	3.38 ± .02	1.71	.013
	"	2	24	5.43 ± .04	3.70 ± .01	.78	.015
	"	3	21	7.30 ± .11	4.10 ± .02		.025
	3-lower	4	5	5.80 ± .10	3.78 ± .06		.023
	"	5	9	7.40 ± .12	4.67 ± .09		(.118)
74-1R				1.48		2.44	
	3-upper	1	21	4.20 ± .06	3.08 ± .02	.97	.018
	"	2	34	6.41 ± .05	3.50 ± .01	.92	.011
	"	3	21	7.12 ± .10	3.67 ± .03		.040
	3-lower	4	10	7.24 ± .05	4.12 ± .07		.083
74-2				1.48		2.62	
	4-upper	1	18	4.06 ± .08	3.30 ± .02	1.55	.008
	"	2	54	5.33 ± .03	3.61 ± .01	2.14	.030
	4-lower	3	7	6.55 ± .13	4.24 ± .08	3.44	.059
	"	4	7	7.83 ± .24	5.03 ± .25		(.304)
74-2R				1.48		2.52	
	4-upper	1	14	4.17 ± .10	3.19 ± .03	1.09	.014
	"	2	57	5.17 ± .03	3.42 ± .01	1.40	.037
	4-lower	3	14	6.59 ± .09	3.88 ± .05	6.36	.153
	"	4	6	7.87 ± .07	5.06 ± .08		.036

(TABLE I)

in Fig. 4.4. These models will be modified in the course of the amplitude analysis discussed in the next section.

4.3 Traveltime and Amplitude Interpretation

COMPUTING SYNTHETIC SEISMOGRAMS

Synthetic seismograms proved valuable for determining a velocity-depth model required by the traveltime and amplitude characteristics of the data. These were calculated according to the recently developed disc ray theory (DRT) of Wiggins (1976), with a computer routine (HRGLTZ) written by R.A. Wiggins. Traveltimes and amplitudes of the synthetic seismograms are calculated from a specified p-Δ curve (described below). The program also performs a Weichert-Herglotz integration of the p-Δ curve to determine a velocity-depth model. Therefore, changes applied to the p-Δ curve while fitting synthetic seismograms to the data also influenced the shape of the velocity versus depth curve.

To generate seismograms which matched the data it was necessary to specify the characteristics of the data in terms of the p-Δ curve. The p-Δ curve refers to a plot of the ray parameter (p) against epicentral distance (Δ). The ray parameter is given by the distance derivative of the traveltime, $dt/d\Delta$, or by $p=r \sin \iota/v$, where r is the distance from the center of the Earth, ι is the angle between the ray and the radius vector, and v is the velocity at r. An initial p-Δ curve can therefore be constructed from the slopes of the

Figure 4.45 Velocity-depth curves determined from first arrival data for each of the four profiles. Datum water depth is 2.4 km. Dashed lines show the calculated water depth determined from the intercept of the first branch. The dotted curves show the down-faulted structures as discussed in the text.

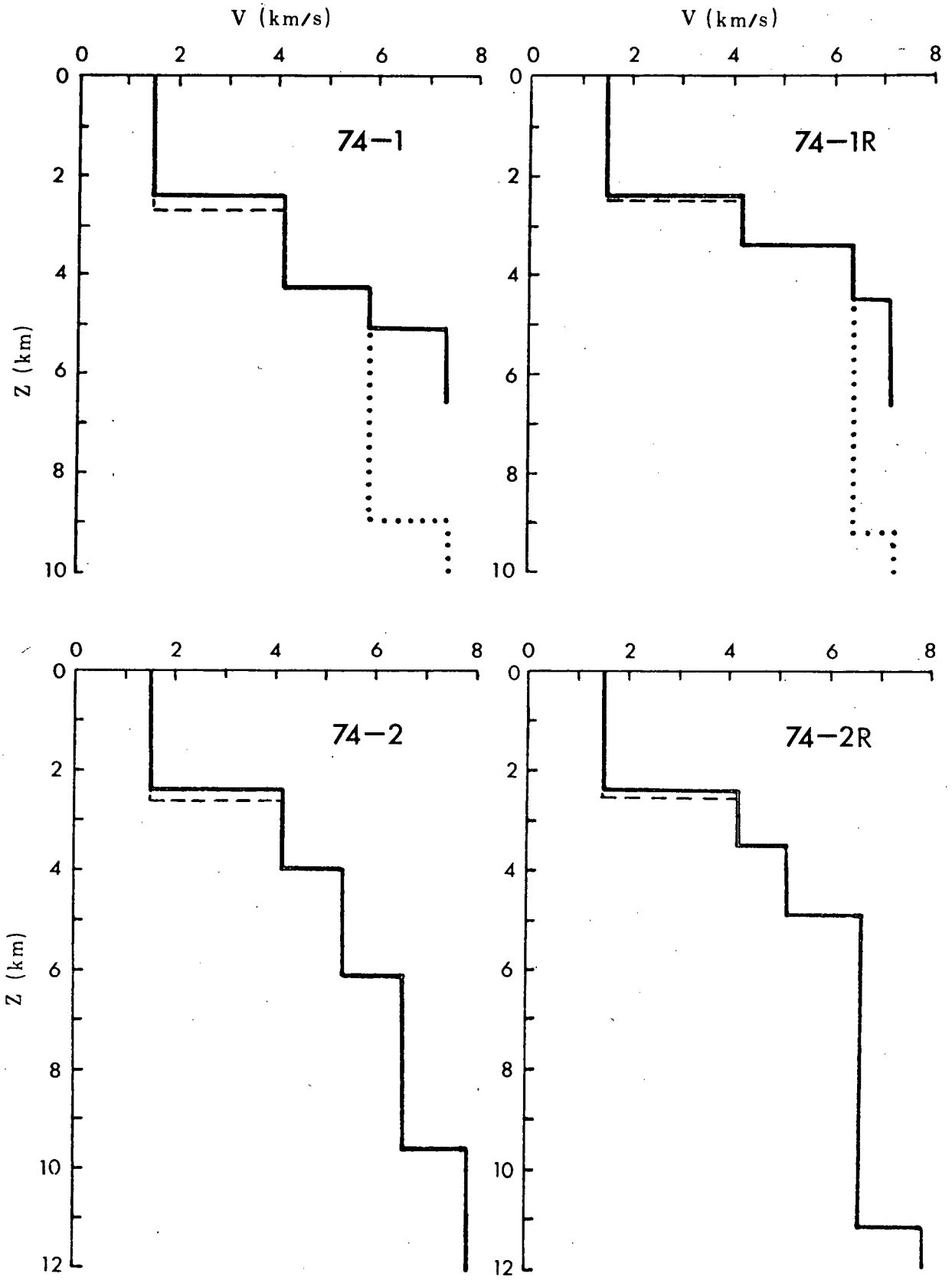
V (km/s)
0
2
4
6
8
Z (km)
74—1
74—1R
74—2
74—2R
10
12

traveltime curves, but since the traveltime curves in Figs. 4.2 and 4.3 show only refraction branches, the portion of the p-Δ curve corresponding to the reflection branches would have to be extrapolated. Although such an approach may have been acceptable, a more convenient method of obtaining an initial p-Δ curve was used. A computer routine (MDLPLT, also by R.A. Wiggins) approximated a continuous Δ(p)[6] curve from a specified velocity-depth curve according to the equations given in Bullen (1965, p. 112). The velocity-depth models determined from the least squares analysis for the four profiles were therefore used to obtain the initial p-Δ curve in each case. For profiles 74-1 and 1R, only the up-fault structures could be specified since the programs are not designed to handle discontinuities such as faults. The continuous p-Δ curves were then "digitized" for subsequent use in HRGLTZ. The sampling interval varied since those parts of the curve showing considerable curvature required more points for the interpolation in HRGLTZ.

After the initial p-Δ curve was constructed, a trial-and-error procedure was used to modify it so that the synthetic record section matched the data. Since both traveltimes and amplitudes were constraints in making the fit, a trade-off between the two was usually necessary. As a result, the traveltime curves fitted with HRGLTZ were not

---

[6] The p-Δ curve is referred to here with Δ as a function of p although it is usually plotted as p(Δ), with p being the ordinate. Since p(Δ) may be multivalued (as it was for these data), Δ(p) correctly expresses the one to one relationship between p and Δ in the absence of low velocity zones.

identical to those obtained from the least squares method.

To serve as a guide for making traveltime and amplitude adjustments with the p-Δ curve, the following relations were borne in mind:

(1) The traveltime, $T(p,\Delta)$, can be written as

$$T(p,\Delta) = p\Delta + \int_{p}^{p_{max}} \Delta(p)dp$$

$$= p\Delta + T(p)$$

where $p_{max} = R/v(R)$ is the maximum p value that can be obtined and R is the radius of the Earth (Wiggins and Madrid, 1974). It was therefore useful to think of the traveltime in terms of the area under the $\Delta(p)$ curve, and a "counting the squares" technique was often used to adjust the traveltime as desired.

(2) The amplitude, $A(p,\Delta)$, is often expressed as

$$A(p,\Delta) = F(p,\Delta)\ |dp/d\Delta|^{\frac{1}{2}}$$

The factor $F(p,\Delta)$ is usually slowly varying compared to $dp/d\Delta$ (Bullen, 1965); hence, the amplitude may be considered proportional to $|dp/d\Delta|^{\frac{1}{2}}$. According to that, a p vs. Δ plot should be steep where large amplitudes are needed and nearly flat for small amplitudes. In practice, more amplitude control was obtained by carefully positioning the Δ ranges where traveltime triplication occurred since the constructive interference of the refracted and reflected phases would cause a large amplitude buildup. This will be illustrated more specifically with the actual data.

Although the procedure was largely by trial and error, the time required to obtain a reasonable fit was greatly

reduced through the use of the Adage graphics terminal at the UBC Computing Center. With the data and synthetic record sections on disk file, the graphics terminal allowed both of them to be shown on CRT display immediately after adjusting the p-Δ curve and running HRGLTZ. This eliminated the need for expensive computer plots which had a lower turn around rate.

APPLICATION OF HRGLTZ TO THE DATA

The manner in which the appropriate p-Δcurves were constructed for the data from the four profiles is now discussed. The synthetic sections computed from these curves should resemble those in Figs. 3.3 through 3.6, at least for the initial 0.5s or so of data. Probable reasons for some of the difficulties encountered during the fitting procedure are also considered. As previously mentioned, HRGLTZ could not be used in the normal way for all of profiles 74-1 and 74-1R; profiles 74-2 and 74-2R are therefore discussed first.

PROFILES 74-2 AND 74-2R

The lower part of Fig. 4.5 shows the p-Δ curve for profile 74-2 based on the simple layered velocity-depth model shown in Fig. 4.4. Synthetic seismograms computed from this curve ($0.46 \leq p \leq 0.12$) at 4 km intervals are plotted with the superimposed traveltime curves on the upper part of the diagram. Since the data had been corrected for spherical spreading, all synthetic amplitudes have been multiplied by the r^2 factor discussed in Sec. 3.4. On all future plots

Figure 4.5 Bottom - The p-Δ curve corresponding to the homogeneous layered velocity-depth model for profile 74-2 (See Fig. 4.4). Top - Synthetic seismograms and traveltime curve computed from the p-Δ curve. Inset shows the source wavelet used for convolution.

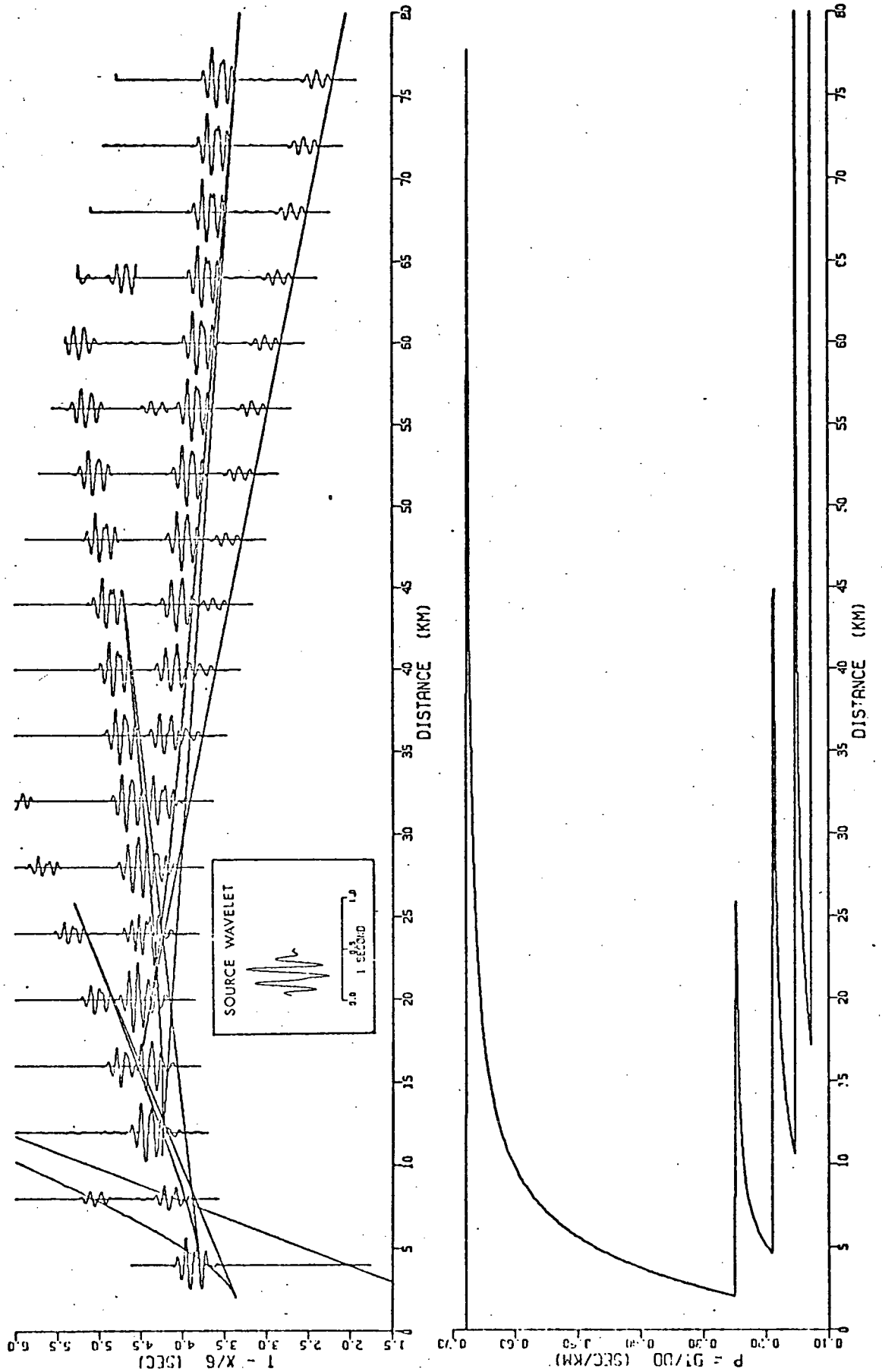
SOURCE WAVELET
1 SECOND
DISTANCE (KM)
T - X/6 (SEC)
P = DT/DD (SEC/KM)
DISTANCE (KM)

of this type, this correction will be assumed. Also, as an attempt to achieve a more realistic waveform, the source wavelet shown in the inset of Fig. 4.5 was convolved with the spiked seismogram computed by DRT at each specified distance (see Wiggins, 1976). This wavelet was used for all record sections and was obtained by simply extracting the first arrival from shot 25 of profile 74-2R (Fig. 3.6).

A comparison of the synthetic record section (Fig. 4.5) and the data record section for profile 74-2 (Fig 3.5) reveals some distinct amplitude differences. Particularly noticeable are the large amplitude secondary arrivals which appear consistently on all synthetic seismograms out to the greatest distances, but no such large amplitudes appear on the data beyond 45 km. The large synthetic amplitudes lie on the reflection branches of the traveltime curve, and since reflections attenuate as $1/r$, the r^2 correction factor exaggerates these amplitudes. However, since the same correction was applied to the data, the decrease in amplitude beginning with shot 35 (44 km) was considered indicative of some real property of the velocity-depth structure. At the nearer distances the abrupt increase in amplitudes on the data at shot 31 (27 km) is also of particular interest since it is not characteristic of the synthetic section.

These differences imply that a simple model consisting of homogeneous layers is not adequate to explain the observed amplitude features. To obtain a more realistic model, the

p-Δ curve was progressively altered until the large amplitudes were approximately confined to the observed range. At the same time attempts were made to preserve the original traveltime fits.

In order to decide on appropriate changes for the p-Δ curve, more attention should be given to the influence of this curve on amplitudes. The previously stated relation, $A(p,\Delta) \alpha |dp/d\Delta|^{\frac{1}{2}}$, suggests a simple way of controlling amplitudes with the p-Δ curve. However, synthetic seismogram amplitudes were found to be much more dependent upon the positions of critical points on the traveltime curve (the distance at which a head wave first exists) than on the slope of the p-Δ curve alone. This observation is consistent with the geometric ray theory prediction that the maximum amplitude for reflected arrivals occurs at the critical point.

To see the relationship between the p-Δ and traveltime curves consider the plots in Fig. 4.5. Critical points on the traveltime curve are located at approximately 2.0, 4.5, 10.5, and 17.0 km for refraction velocities of 4.06, 4.33, 6.55, and 7.83 km/s, respectively. These distances also locate the corners of a series of lens shaped curves comprising the p-Δ curve. The bottom part of the lens corresponds to refraction arrivals, with the highest velocities being associated with the lowest p values. The upper part of the lens corresponds to reflected arrivals ranging from near critical to wide angle.

For homogeneous layers the reflection and refraction branches are asymptotic although Fig. 4.5 does not clearly illustrate this fact. By allowing these curves to become tangent to each other at some finite distance however, the large reflection amplitudes which start at the critical point can be terminated where desired. Large amplitudes will then be confined, for the most part, to the region between cusps on the traveltime curve, or equivalently, the zone of traveltime triplication.

Fig. 4.6 illustrates how this criteria for fitting amplitudes was used to adjust the p-Δ curve for each layer. The process involved moving the endpoints (Δ values) of the traveltime triplication according to where large amplitudes appeared on the data. For profile 74-2 however, the last two triplications are barely discernible. Recalling that the traveltime is equal to the area under the $\Delta(p)$ curve, it is clear that such changes would alter the traveltime unless both endpoints had been moved in opposite directions by the correct amount. Compensation was therefore made by either increasing or decreasing the thickness of the lens shaped curves for the layers concerned although changing the slope did have an additional effect on amplitudes.

Fig. 4.7 shows the p-Δ curve before (dashed line) and after (solid line) being adjusted for a traveltime and amplitude fit. The change in the position of the critical point was greatest for the last two refractors ($p = 0.152$ and $p = 0.127$). To compensate for the large increase in

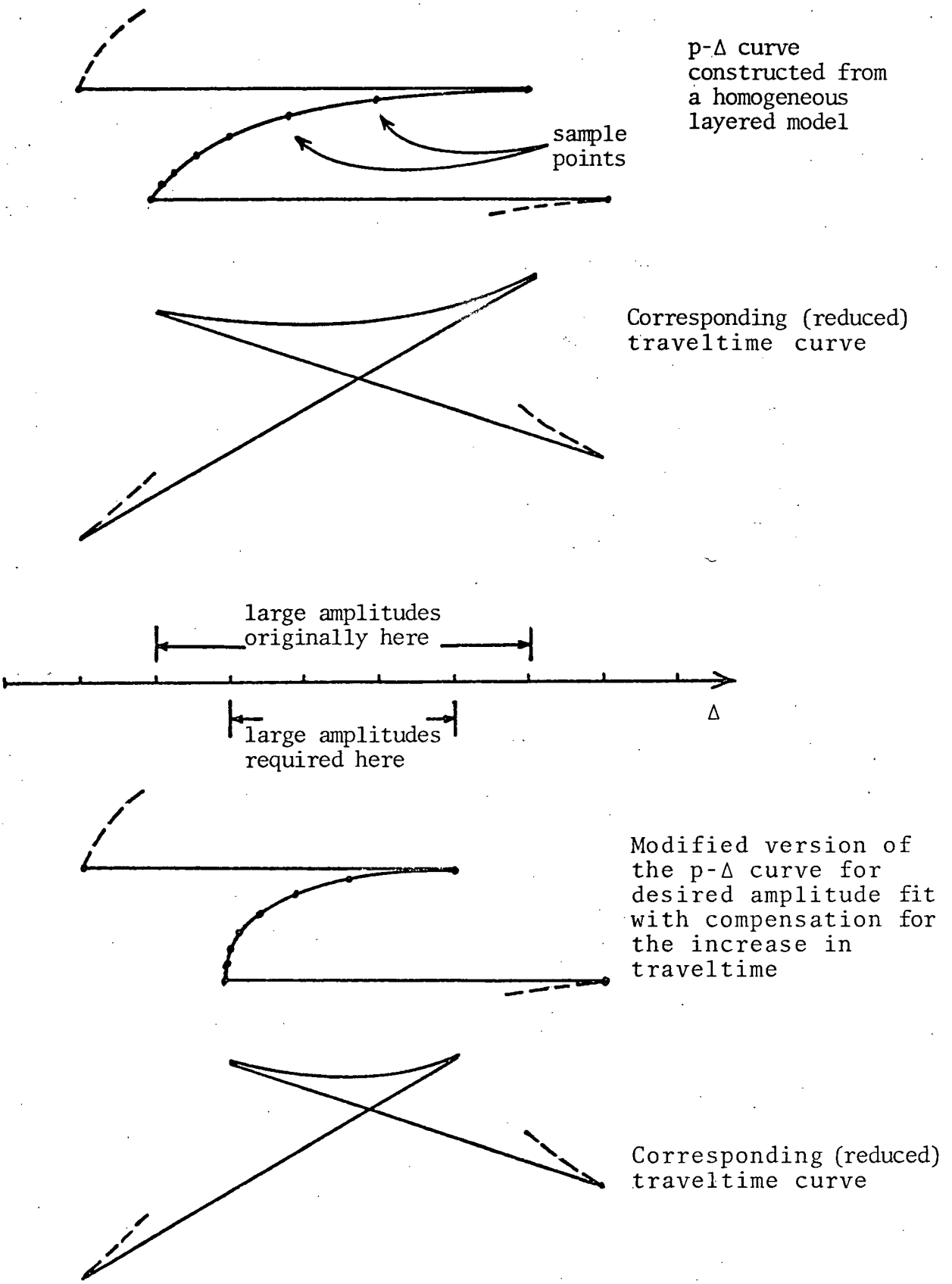

Figure 4.6 The procedure used in adjusting the p-Δ curve to control the amplitudes of synthetic seismograms.

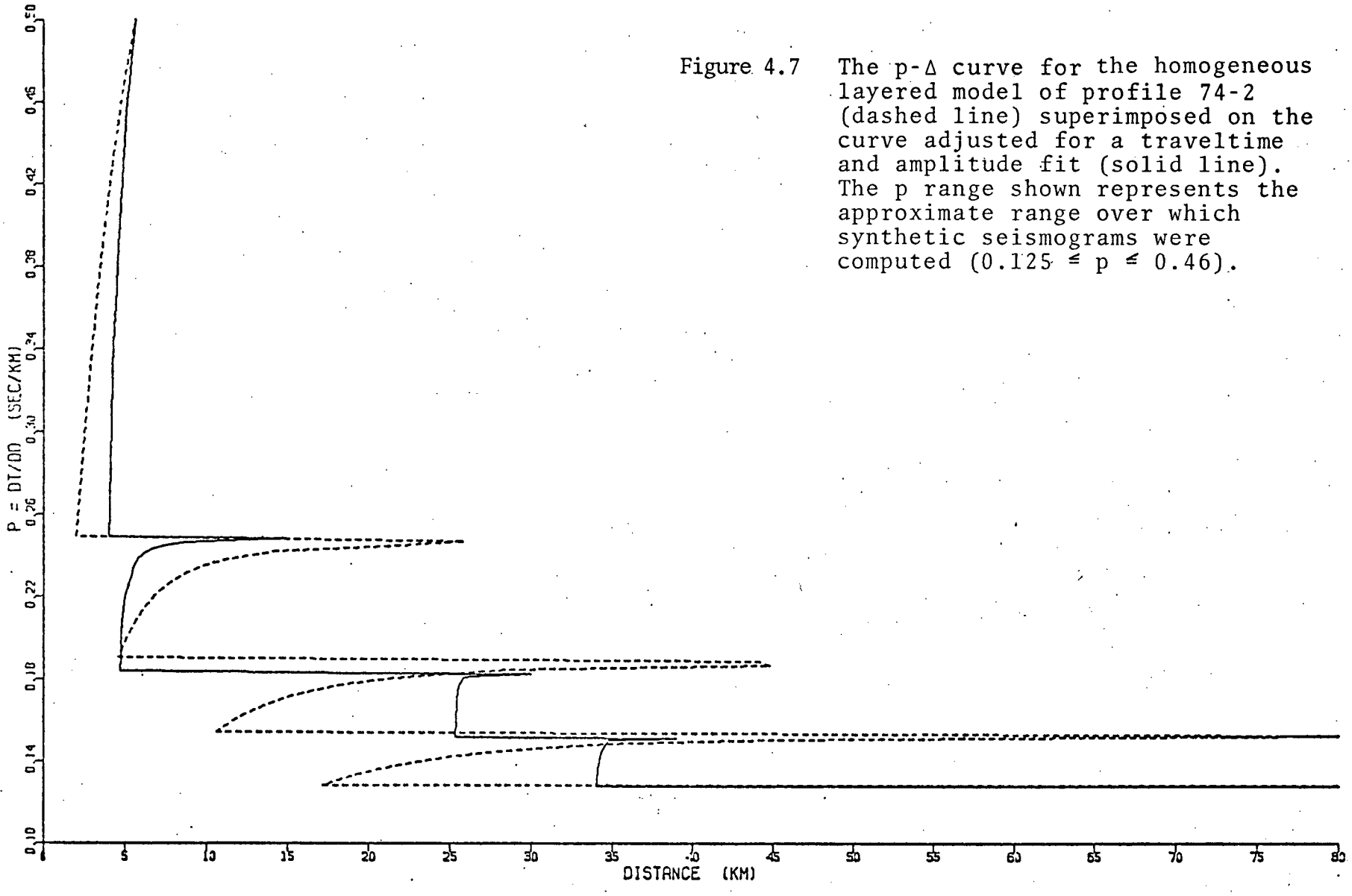

Figure 4.7 The p-Δ curve for the homogeneous layered model of profile 74-2 (dashed line) superimposed on the curve adjusted for a traveltime and amplitude fit (solid line). The p range shown represents the approximate range over which synthetic seismograms were computed ($0.125 \leq p \leq 0.46$).

traveltime accompanying this change, the respective "lenses" were thickened as much as possible. As a further attempt to lower the traveltime the refraction velocity of an overlying layer was increased slightly, or as shown in the diagram, the p value was decreased by a constant amount.

The synthetic seismograms computed from the revised p-Δ curve and a truncated version of the record section for profile 74-2 are shown in Fig. 4.8. Both are plotted on the same scale and have identical traveltime curves superimposed.

The problems discussed with the construction of the p-Δ curve are readily apparent in Fig. 4.8. The largest amplitudes on the synthetic section begin around 24 km rather than 27 km as observed on the data. Also, the calculated traveltime along the refraction branches beyond 24 km are too long while those before 24 km are generally too short to fit the first arrivals. These difficulties illustrate the traveltime-amplitude trade-off that had to be made to obtain a reasonable fit.

To be sure, experimental errors account for some of the difficulties with fitting. The results of a theoretical study of reflection and head wave amplitudes by Červený (1966) may, however, provide a further explanation. He showed that the amplitudes of reflected arrivals near the critical point do not reach a maximum until some distance beyond the critical point where the reflected wave and head wave interfere. This distance is between 10 and 50 km depending on the frequency of the reflected wave; it is larger for low frequencies

Figure 4.8 Top - Synthetic seismograms and the traveltime curve computed from the modified p-Δ curve shown in Fig. 4.7. Bottom - Data from profile 74-2 (approximately 1.8s of each trace). with the traveltime curve of the upper diagram superimposed.

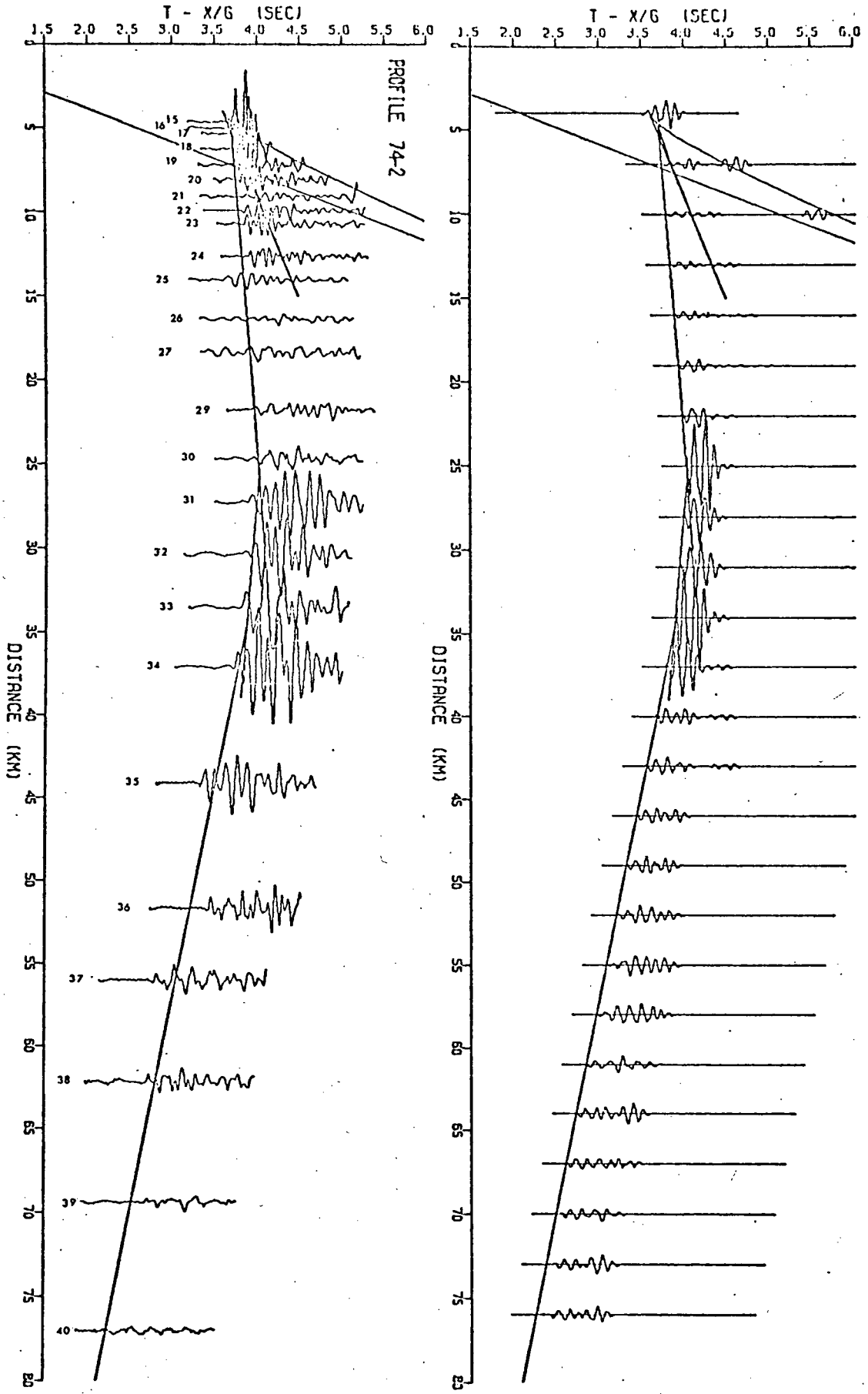
T - X/G (SEC)
1.5 2.0 2.5 3.0 3.5 4.0 4.5 5.0 5.5 6.0
PROFILE 74-2
DISTANCE (KM)
0 5 10 15 20 25 30 35 40 45 50 55 60 65 70 75 80
15
16
17
18
19
20
21
22
23
24
25
26
27
29
30
31
32
33
34
35
36
37
38
39
40

and smaller for high frequencies.

Three of the seismograms which have large amplitudes (shots 31, 32, 33) were used to determine the 6.55 km/s branch from the first arrival data (Fig. 4.3). The critical distance for this branch is certainly less than the crossover point (17 km) with the 5.17 km/s branch. The distance between the critical point and the large amplitudes is then at least 10 km. However, since the critical point had to be placed at 24 km to obtain large amplitudes there, its position is not correct according to the original traveltime fit. In other words, using the geometric ray theory criteria to generate large amplitudes has displaced the critical point and increased the traveltime by more than what could be compensated.

A similar situation exists with the least squares determined 7.83 km/s branch. According to its point of intersection with the 6.55 km/s branch, the critical distance is less than 31 km. Again, the critical point was placed at a greater distance (34 km) to produce amplitudes similar to those on the data. In this case though, the traveltime increase will also include the increase on the previous (6.55 km/s) branch.

Although the above discussion has pointed out the difficulties experienced in using the critical point criteria to fit large amplitudes, it should be remembered that crossover points (and therefore critical points) were not well determined on the data. Crossover points in the least

squares analysis were quite dependent upon which points were included on a particular branch. This is especially true at larger distances where fewer data points were available and assigning two or three data points differently could shift the crossover point by 5 km or more.

The amplitude fit along the last traveltime branch is good except for the last two shots where the data suddenly appear more attenuated. For these shots however, the largest charge size was used (three projectiles), and since the energy yield of the projectiles was not well known, the charge size correction factor may have been excessive. At the near distances though (<25 km), the first arrival amplitudes are reasonably well fit.

The procedure for determining the p-Δ curve for profile 74-2R was the same as for profile 74-2 described above. The resultant curve was, however, significantly different. The main reason for the difference was the contrasting nature of the traveltime curves as shown by Fig. 4.3.

A comparison of the record sections for profiles 74-2 and 74-2R (Figs. 3.5 and 3.6) shows that the amplitude characteristics of these profiles are quite similar. Large amplitudes were again observed over a limited region for profile 74-2R, but in this case, their onset was more gradual. That is, increased amplitudes were observed as early as 21 km, but the maximum didn't appear until about 30 km. As with profile 74-2, there was a definite fall-off

in amplitudes beyond a certain distance, in this case, 43 km (shot 35). Although only large projectiles were used after shot 35 (as the higher frequency in shot 36 might suggest), the decrease in amplitude was considered significant in terms of crustal structure.

Fig. 4.9 shows the data and synthetic seismograms for profile 74-2R with the traveltime curve superimposed on each. Many of the same problems discussed with profile 74-2 were encountered again. The large amplitudes extending beyond 50 km on the synthetic section were particularly difficult to reduce in size. For this profile all large amplitudes were generated over the range of one triplication beginning at the critical point of the last refraction branch. Therefore, moving the large amplitudes further to the left would have meant decreasing traveltimes on the last refraction branch more. The situation is actually opposite to what it was for profile 74-2 in that the critical point has been moved to the left by too much to be adequately compensated. Again, however, it is important to realize the range in possible positions for the crossover points that would tend to "soften" these difficulties. For this profile as well, first arrival amplitudes for the smaller distances (< 25 km) have been fit well.

PROFILES 74-1 AND 74-1R

Because of the offset and delay of the 7.3 km/s branch on profiles 74-1 and 74-1R, a continuous p-Δ curve could not

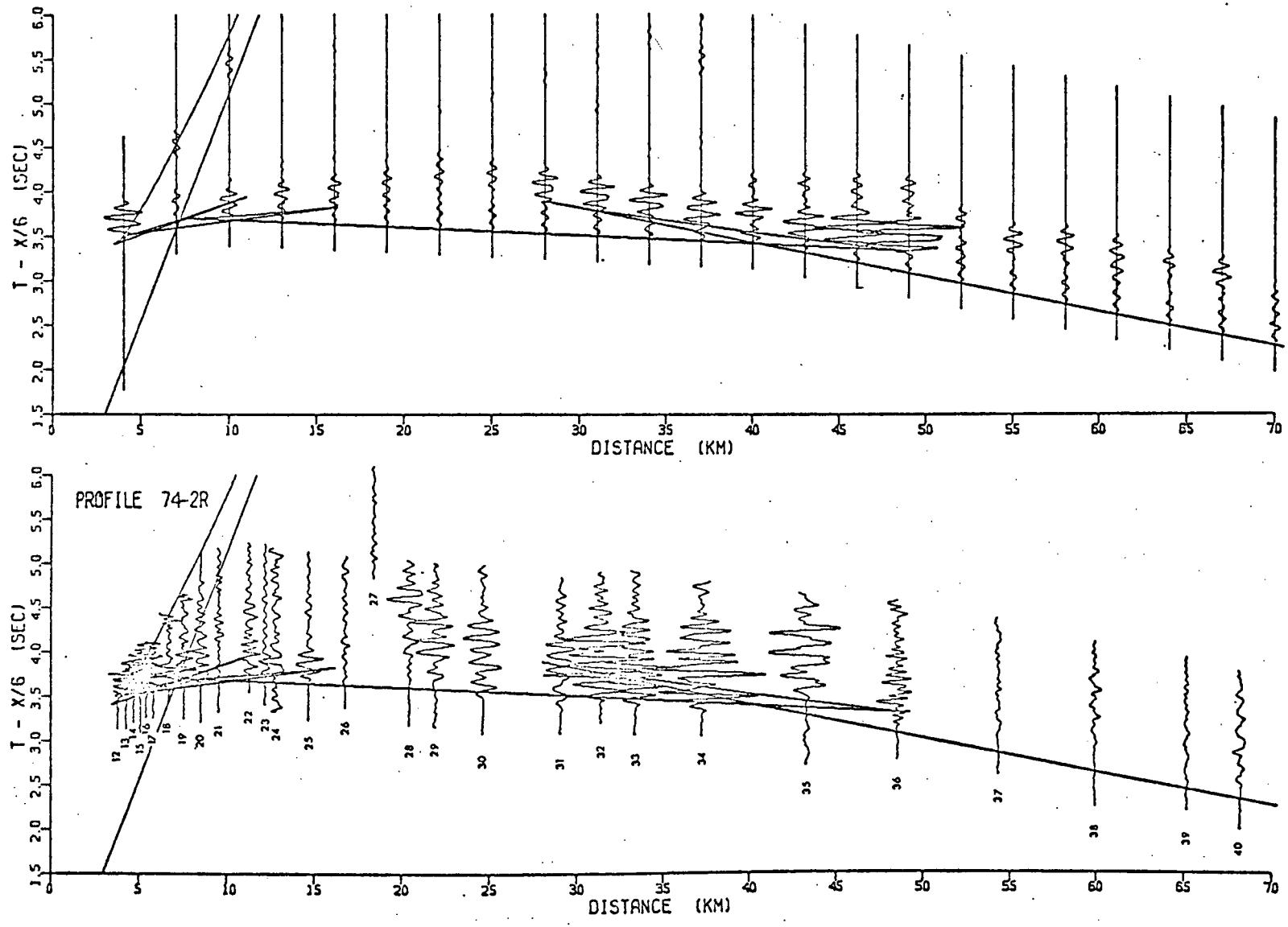

Figure 4.9 Same as Fig. 4.8 for profile 74-2R.

be constructed for either profile. Although HRGLTZ can be used to obtain synthetic seismograms from a discontinuous p-Δ curve (the same p value for two different Δ), the physical interpretation of the discontinuity is then a low velocity zone. For a lateral discontinuity such as a fault, HRGLTZ cannot be used to produce meaningful seismograms beyond the fault. Thus, for profiles 74-1 and 74-1R which show evidence for faulting on the Moho, synthetic seismograms were computed for the up-fault structures only ($\Delta < 25$ km)

Fig. 4.10 shows the data from the two profiles over the up-fault region with the associated synthetic sections and traveltime curves displayed in their usual manner. As with profiles 74-2 and 74-2R, the well defined first arrivals and uniform amplitudes at near distances allowed a good traveltime and amplitude fit to be made.

Although synthetic seismograms were not computed for the latter part of either profile, it is interesting to note that the large amplitudes characteristic of profiles 74-2 and 74-2R also appear on profile 74-1R within approximately the same distance interval (30-50 km) (see Fig. 3.4). The data from profile 74-1, on the other hand, show no such prominent feature (see Fig. 3.4). The large amplitudes on shot 37 are regarded as anomalous, probably caused by an error in the amplitude correction factor.

Despite the limitations on the amplitude analysis for these profiles, HRGLTZ could be used for fitting

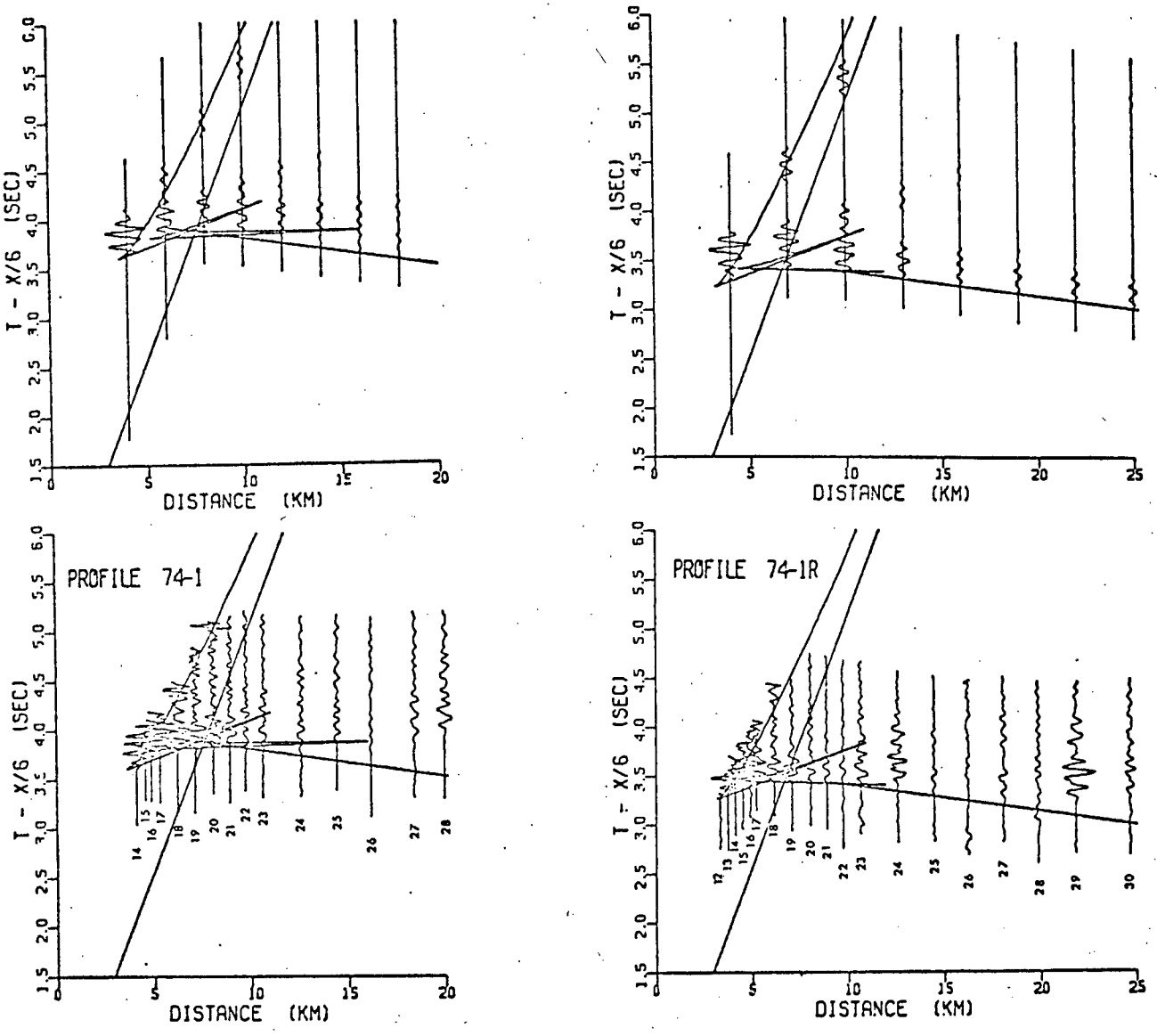

Figure 4.10 Same as Fig. 4.8 for up-fault regions of profiles 74-1 (left) and 74-1R (right).

traveltimes beyond the fault. The throw of the fault was then determined from the difference between the up-fault and down-fault velocity-depth structures. The method used follows the one developed by Bennett (1973).

Since HRGLTZ computes horizontal layers only, the fault throw must be thought of in terms of an increase in layer thickness. For a normal fault, simple geometric ray theory shows that the time delay due to the fault will be less than the delay due to increasing the layer thickness by the amount of the fault throw. Therefore, to calculate the down-fault structure with HRGLTZ, a time correction ΔT expressing this difference must be obtained. The details on calculating ΔT, assuming a fault on the Moho only, are given in the Appendix. For profiles 74-1 and 74-1R the ΔT values were 0.261s and 0.235s, respectively.

The down-fault p-Δ curve was then constructed from the up-fault version that had been determined using synthetic seismograms. For a faulted Moho, the area under the $\Delta(p)$ curve was increased according to the above stated ΔT values within the p range applicable to Moho reflections and head waves. Since there were no amplitude constraints imposed while making the change, the shape of the lowest part of the p-Δ curve was completely arbitrary. However, unlike the traveltime integral, the depth integral is weighted. Thus, some reasonable shape was maintained for the final lens of the p-Δ curve.

FINAL VELOCITY-DEPTH MODELS

The final velocity-depth models obtained after fitting arrival traveltimes and amplitudes of the data for the four profiles are presented graphically in Fig. 4.11. These should be compared with the models obtained from the traveltime interpretation alone (Fig. 4.4). The most obvious change in each case involves going from a crustal model composed of homogeneous layers to one where positive velocity gradients exist within the layers. The change is most drastic for profile 74-2 where the velocity discontinuity in the lower crust has been nearly eliminated. The gradients shown for the down-fault models of 74-1 and 74-1R (dashed lines) are, however, not significant since no amplitude control was maintained while adjusting the p-Δ curve.

Besides being intuitively more realistic, the velocity gradients also explain some of the amplitude features on the data. Červený and Ravindra (1971) describe a wave called an interference head wave which is caused by a positive velocity gradient below a plane interface. Although the kinematics of these waves are similar to those of pure head waves, i.e. the traveltimes are nearly the same, the amplitude and spectral characteristics are very different. Even for small gradients (0.01 km/s/km) interference amplitudes may be one or two orders of magnitude larger than the amplitudes of pure head waves (Červený, 1966). The models in Fig. 4.11 show that a gradient of about 0.30 km/s/km exists in the lower crust for profile 74-2 and about 0.10 km/s/km for profile 74-2R. In light of the preceding discussion, these gradients seem to be a likely explanation for the large

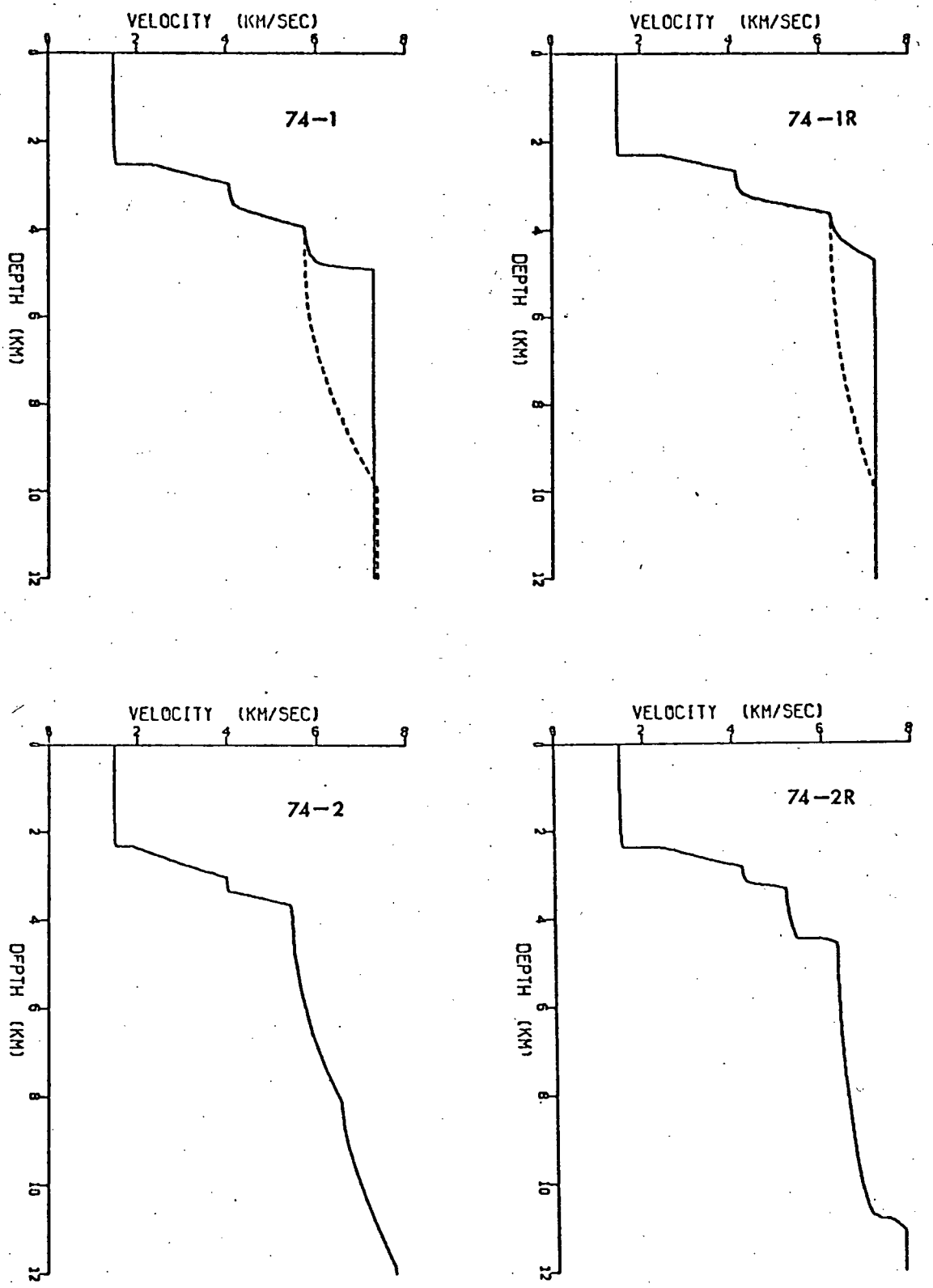

Figure 4.11 Velocity-depth curves determined for each of the four profiles by fitting both traveltimes and amplitudes with synthetic seismograms. Dashed lines represent down-fault structures.

amplitudes appearing at approximately 30 km on the record sections.

The velocity gradients may also account for the decrease in amplitudes beyond 50 km. At these distances a gradient may be producing a shadow zone for Moho reflections (Červený and Ravindra, 1971). As a result, the interference head wave will no longer exist.

In the course of adjusting the p-Δ curve to fit amplitudes the layer thicknesses were altered from their least squares values. The differences are generally less than 0.20 km, except for profile 74-2 where the thickness of the second crustal layer was increased by more than 2 km. The total crustal thickness for profile 74-2 (including 2.40 km of water) was then 11.8 km, which agrees favorably with the 11.2 km for profile 74-2R.

For profiles 74-1 and 1R, a down-fault crustal depth of 9.9 km was computed. This increases the respective fault throw values to 4.5 and 5.1 km from the earlier values of 3.9 and 4.7 obtained from the traveltime calculation.

A more complete discussion of these models is given in Chapter 5 where their geological significance is considered.

LATER DATA

Although the traveltime and amplitude analysis of this study was primarily concerned with the first 1.0s of data, it was interesting to observe that the large amplitudes characteristic of first arrivals between 30 and 50 km consistently reappeared at a later time on the record sections.

The data from profile 74-2 are taken as an example of this and are again presented in record section form (Fig. 4.12). The onset of the large amplitudes initially occurs at approximately 3.5s reduced traveltime. Although the amplitudes are somewhat attenuated, the waveform is much the same for arrivals at approximately 7.0s. A simple explanation for this observation is that the later arrivals represent multiple phases, i.e. due to energy which has reflected once from the water surface before penetrating the substratum. To check this possibility, the two-way normal incidence traveltime of 3.24s (assuming 2.4 km datum and 1.48 km/s water velocity) was added to relevant sections of the superimposed traveltime curve obtained with the HRGLTZ routine. As Fig. 4.12 shows, this procedure resulted in branches which fit the traveltimes of the large amplitude secondary arrivals reasonably well. At greater distances such a fit is not clearly evident. A prominent feature of the data beyond 45 km (shot 35) is the presence of strong arrivals which appear to be multiples of secondary phases. A more detailed interpretation including these later secondary phases may reveal their significance.

Figure 4.12 Record section of data from profile 74-2 with the superimposed traveltime curve determined with HRGLTZ (lower curve) and a set of refraction branches delayed by the normal incidence two-way traveltime (3.24s), assuming a water depth of 2.4 km (upper curve). The resultant fit implies that later arrivals are multiples.

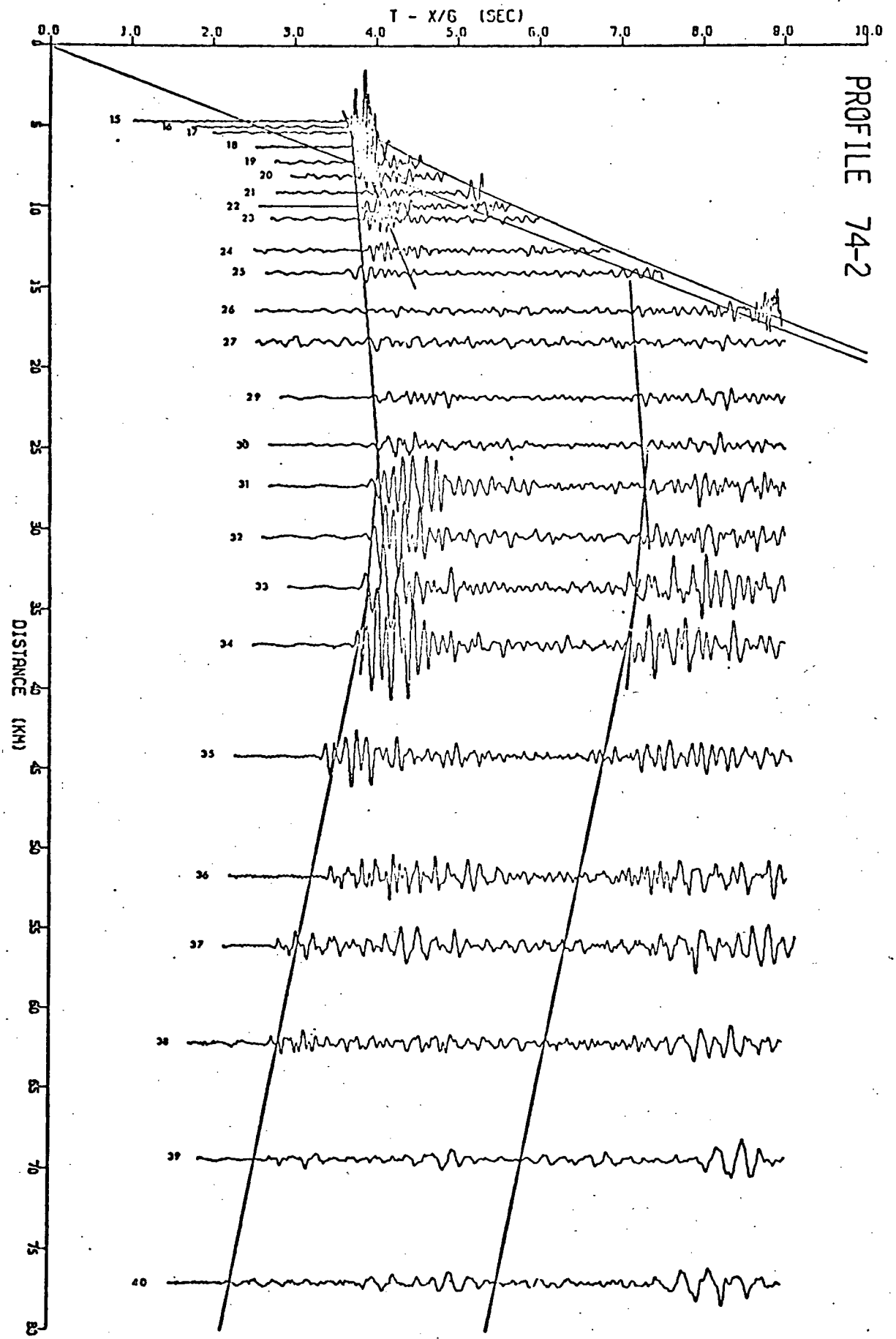
T - X/6 (SEC)
0.0
1.0
2.0
3.0
4.0
5.0
6.0
7.0
8.0
9.0
10.0
PROFILE 74-2
DISTANCE (KM)
0
5
10
15
20
25
30
35
40
45
50
55
60
65
70
75
80
15
16
17
18
19
20
21
22
23
24
25
26
27
29
30
31
32
33
34
35
36
37
38
39
40

5. DISCUSSION OF RESULTS

5.1 Determining a Petrologic Model

To discuss more completely the models obtained from the traveltime and amplitude analysis, a petrologic model consistent with these results is first sought. A satisfactory petrologic model must, however, take into account not only seismic structure, but also the lithologies of seafloor dredge samples and the results of seismic velocity measurements on these samples (Christensen and Salisbury, 1975). Since ophiolites are regarded as allochthonous slabs of oceanic crust that have been emplaced on the continental margins (Coleman and Irwin, 1974), the importance of relating the ophiolites to a petrologic model must also be recognized.

Since no dredge sample analysis accompanied the DSS study, it is worthwhile considering other seismic results and the petrologic correlations that have been made with them. The analysis of refraction data by Raitt (1963) has implied a relatively simple seismic structure for "normal" oceanic crust. Velocity and thickness values of Raitt's model for the crust below the usually thin (< 1 km) sedimentary layer are given in Table II. More recently, detailed sonobuoy refraction studies have refined this model somewhat. Profiles conducted by Talwani et al, (1971) over the Reykjanes Ridge have indicated that layer 2 is composed of

TABLE II*

Raitt's Seismic Model			Revised Model Based on Sonobuoy Data			Petrologic Model	
Layer	Velocity (km/s)	Thickness (km)	Layer	Velocity (km/s)	Thickness (km)	Layer	Lithology
			1 (sediments)	1.7-2.0	0.5	1	unconsolidated sediments
2 (basement)	5.07 ± 0.63	1.71 ± 0.75					
			2A	2.5 - 3.8	0.5 - 1.5	2A	(fractured) basalt flows and pillows
			2B	4.0 - 6.0	0.5 - 1.5	2B	metabasalt, diabase
3 (oceanic)	6.69 ± 0.26	4.86 ± 1.42					
			3A	6.5 - 6.8	2.0 - 3.0	3A	gabbro
			3B	7.0 - 7.7	2.0 - 5.0	3B	(cumulate) gabbro and peridotite
Mantle	8.13 ± 0.24		Mantle	8.1		Mantle	peridotite

* Velocity-depth models for the oceanic crust based on early refraction results (after Raitt, 1963) and the results of more recent sonobuoy data (after Peterson et al, 1974). The petrologic model correlated with the seismic layers is similar to the model given by Peterson et al (1974).

two velocity layers. Studies by Sutton et al (1971) have revealed the presence of a high velocity basal crustal layer in the Pacific Basin meaning that layer 3 should also be subdivided. Although the quantity of sonobuoy data is limited, the fairly consistent occurrence of these velocity subdivisions has led to a modification of Raitt's model. The nomenclature 2A and 2B, and 3A and 3B has subsequently been introduced to specify the subdivisions. A seismic crustal model based on sonobuoy data has been constructed by Peterson et al, (1974) and is also shown in Table II.

Owing to the complex nature of the geologic processes responsible for the evolution of the oceanic crust, no single petrologic model has been found which consistently accounts for the geophysical and geological data obtained in all situations. Various models have been proposed among several researchers on the basis of seismic results together with data collected from dredge samples (e.g. Christensen, 1970; Cann, 1970) or from the ophiolite complexes (e.g. Peterson et al, 1974; Moores and Jackson, 1974). No attempt will be made here to review in detail the proposed models, or point out their differences. But for the purpose of discussing the velocity depth curves in Fig. 4.11, a petrologic model similar to the one described by Peterson et al, (1974) will be assumed. The model is presented in Table II and is intended to be quite general. The lithologies include a broad range of rock types, e.g. peridotite, and no depth has been specified although a

scale is implied by the indicated correlations with the seismic layers.

5.2 The Oceanic Crust in the Region of Explorer Ridge

The velocity-depth models derived from the seismic data are combined with the petrologic model of Sec. 5.1 and the tectonics involving Juan de Fuca plate, to present a more complete description of the crust in the region of Explorer Ridge. Although the discussion is organized according to the layer sequence commonly associated with the oceanic crust, it should be emphasized that the models of Fig. 4.11 do not suggest homogeneous layers. The velocity gradients were introduced by fitting both traveltimes and amplitudes during the interpretation procedure. Therefore, the term "layer" used in other models will now correspond to the depth interval where the velocity gradient is continuous.

UPPER CRUSTAL STRUCTURE

All four velocity-depth models in Fig. 4.11 show that the immediate sub-bottom material has a very high velocity gradient - the velocity increases from 2.5 to 4.2 km/s over a 0.5 km interval. Since velocities over 3 km/s are not characteristic of sediments, the sedimentary cover is considered minimal. That there are little sediments is also confirmed by the calculated water depths. As the diagrams show (see Fig. 4.4 or Fig. 4.11), these range from

2.4 to 2.6 km and compare favorably with the datum of 2.4 km. In addition, the lack of penetration on continuous seismic profiling in the region indicates that the acoustic basement (below the sediments) is the predominant sub-bottom feature with some isolated areas containing a thin veneer (< 250 m) of sediments (A.G. Tomlinson, pers. comm., 1975).

From 0.5 to 1.0 km sub-bottom, the velocity has a nearly constant value of 4.2 km/s. The gradient increases considerably over the next 0.4 km, as the velocity (depending on the profile) reaches 5.2 - 6.3 km/s at about 1.4 km.

The 1.4 km of crust discussed so far can be associated with layer 2A, the upper part of the basaltic layer. For most of this depth, the range in observed velocities is nearly the same as the 2.5-3.8 km/s range obtained from the analysis of basalt dredge samples (Peterson et al, 1974). The low seismic velocities and large gradients within the upper 0.5 km may be due to cracks and pore spaces in the pillow basalts as suggested by Matthews et al (1971). As they point out, velocities are strongly influenced by cavities in rocks when confining pressures are less than 1 kbar. Therefore, at depths where the hydrostatic pressure is greater than 1 kbar, the velocity will show a smaller change with increasing depth. This may explain the nearly constant velocity (4.2 km/s) observed over the next 0.5 km. Also, extensive fracturing may have taken place only in the uppermost part of the crust to account for the limited range of the lowest velocities. Support for these ideas may be claimed

from dedging results in an area near the profile lines of this study. For example, vesicular pillow lavas have been dredged from the northern end of Explorer Ridge near Paul Revere Ridge, (Srivastava et al, 1971). At the southern end, on the Sovanco fracture zone, pillows and pillow fragments comprise many of the basalt samples obtained there (Barr and Chase, 1974).

For profiles 74-2 and 2R a velocity of about 5.4 km/s is noted at a depth of 1.4 km, while for 74-1 and 1R the velocity is closer to 6.0 km/s at approximately the same depth. With the exception of 74-2 and the down-fault structures of 74-1 and 1R, these values change only slightly over the next 1.0 km interval. These velocities are within the range of laboratory measured velocities (4.0 - 6.0 km/s) (Peterson et al, 1974) for metabasalts which are proposed to constitute layer 2B. In this case no dredge sampling results were available to support the presence of such rocks. However, the youth of the pillow lavas and the high heat flow values obtained in the vicinity of Explorer Ridge (Lister, 1972) imply that high thermal gradients are present and could produce such low-grade metamorphism in the basaltic layer. Therefore, if this 1.0 km layer is assumed to correspond to layer 2B, the total thickness of the layer 2 system is around 2.5 km. Such a thickness is greater than the median value of 1.4 km for the Pacific Ocean but not unique (c.f. Shor and Raitt, 1969). The fact that such results are obtained in the vicinity of young crust is interesting and

will be commented on later.

THE LOWER CRUST AND MOHOROVIČIĆ DISCONTINUITY

The models of Fig. 4.11 imply that the velocity-depth structure is much more varied in the lower part of the crust than it is in the upper part. For profile 74-2R velocities characteristic of the layer 3 system of Peterson et al, (1974) are found over a 6.6 km interval. For 74-2, where gradients are more pronounced throughout the lower crust, it is difficult to decide on a layer 3 equivalent. If the small discontinuity in the gradient at approximately 8 km is interpreted as a layer 2 - layer 3 boundary, the layer 3 thickness would be around 3.7 km. This would mean a difference of almost 3 km between thickness values obtained from two profiles, both of which cross the ridge. Hence, it is probably more appropriate to simply consider the gradient continuous, as it is for 74-2R, and assume that the 1.0 km thick layer 2B interpreted on other profiles is not discernible. If the upper 1 km of the gradient is considered part of layer 2, a thickness of about 6.9 km could be taken as the average value for the layer 3 system below the ridge. The essential difference between the velocity-depth models of profiles 74-2 and 74-2R would then be the shape of the gradient in the lower crust. For 74-2R the velocity changes by only 1 km/s over a 5.5 km interval and then increases to 7.8 km/s within 1 km. With 74-2, on the other hand, the velocity increases steadily from 6.0 to 7.8 km/s over the entire depth range associated with layer 3.

Since profiles 74-2 and 2R are reversed and extend to nearly 80 km, the 7.8 km/s obtained at a depth of 11.8 km for 74-2 and 11.2 km for 74-2R is taken as the medium velocity of the uppermost mantle in the direction perpendicular to the ridge. An average of 9.1 km is therefore obtained for the total sub-bottom crustal thickness near the ridge crest. Such a value is inconsistent with the results of surveys near other axial zones in which a thinner crust of the order of 4.4 km sub-bottom is determined (LePichon et al, 1965; Keen and Tramontini, 1970; Poehls, 1974). However, in a study of the Pacific basin northwest of Explorer Ridge, Srivastava et al, (1971) have interpreted seismic refraction data to show a crustal section with a layer 3 thickness of 5.5 km and a depth below sea level to the Moho of about 11 km. These values are similar to those for the average Pacific basin crust (Shor and Raitt, 1969) and also agree reasonably well with the depths (not velocities) from profiles 74-2 and 2R.

The similarity of the crustal depth from this study and that of Srivastava et al, (1971) may be relevant to some of the ideas regarding plate tectonics in the northeast Pacific. McManus et al, (1972) propose that the northwest-salient block of the Juan de Fuca plate (region between Juan de Fuca and Explorer ridges) is being severed from the remainder of the plate due to the reorientation of Explorer Ridge which began about 7.5 m.y. ago. The Queen Charlotte Fault may now extend south to intersect the northern end of Juan de Fuca Ridge (McManus et al, 1972; Barr and Chase, 1974)

meaning that Explorer Ridge is no longer an active spreading center. If such a situation exists, the region of the ridge would be expected to cool since that time enabling a more usual northeastern Pacific crust to evolve in the vicinity of the (currently inactive) ridge crest. One questionable aspect of this suggestion is, however, whether a period of less than 1 m.y. since the most recent spreading took place is sufficient for the crust to evolve to this extent. Due to the complex geology and tectonics associated with a spreading center, this is not readily answerable.

For profiles 74-1 and 1R the lower velocity-depth structure shown in Fig. 4.11 is more complicated than it is for 74-2 and 2R. Both the up-fault (solid curves) and down-fault (dashed curves) structures are shown, and they indicate fault throws on the 7.3 km/s refractor of 4.9 and 5.1 km for 74-1 and 1R, respectively. Although the profiles were reversed and the medium velocity for the deepest penetration of the rays was well determined out to 80 km, it was questionable as to whether an upper mantle velocity had been observed. In other words, do the models represent faults on the Moho? The interpretation of this velocity was of further importance since a velocity of 7.3 km/s must be regarded as anomalously low for the upper mantle. It is, however, within the range of velocities determined in other refraction surveys near ridge crests (LePichon et al, 1965; Keen and Tramontini, 1970).

One way of resolving the question was to assume that 7.3 km/s was a velocity of the lower crust and calculate the depth to Moho for a 7.8 km/s upper mantle in which head waves are recorded as first arrivals at a distance of 80 km and beyond. Using the velocity and layer thickness values from the traveltime model (Table I), a computed Moho depth of 18.7 km was obtained. This value is well outside the 10-12 km range normally associated with the oceanic crust and was therefore considered unrealistic.

Regarding 7.3 km/s as an upper mantle velocity implies that the crust is extremely thin on the up-fault structure, about 2.6 km sub-bottom, or 5 km total. Also, in the up-fault structure, layer 3 velocities appear to be missing or slow, e.g. the velocities around 5.8 and 6.2 km/s for profiles 74-1 and 1R, respectively. The thick layer 2 system noted in the previous discussion, and the low layer 3 velocities observed here may be due to a thermal depression of layer 3 velocities as suggested by Christensen and Salisbury (1975). They conclude that abnormal layer 2 thickness, a thin or absent layer 3, and the presence of abnormal mantle velocities are interrelated phenomena at many young sites. Another possibility is that extensive fracturing, perhaps related to faulting, has occurred in layer 3 and decreased the seismic velocities.

As pointed out earlier, the shape of the gradient which extends to the Moho on the down-fault structures of profiles 74-1 and 1R is not necessarily realistic, since

both traveltimes and amplitudes could not be used to constrain this portion of the model. Therefore, it is difficult to say whether velocities characteristic of layer 3 are present over any appreciable depth extent in the down-faulted region. Based on the location of profile lines (Fig. 1.1), the lower velocity-depth structure in the down-faulted region of 74-1R should be similar to the structure determined from 74-2. However, a Moho depth of 11.8 km was obtained from 74-2 while the down-fault depth from 74-1R was only 9.9 km. Part of the difference may be due to the fact that 74-2 reached the deep crustal structure closer to the ridge than 74-1R did. The errors associated with the velocities used in computing delay times for modelling the fault may further account for this difference.

The faults proposed in the region of profiles 74-1 and 74-1R represent a significant result of the data interpretation. Some attention is now given to the geologic and tectonic evidence which support a fault model. Evidence based on the seismic observations was mentioned in Sec. 4.2.

According to the first arrival data discussed in Sec. 4.2, the proposed faults should be present in the region near the start of each profile (< 25 km). For profile 74-1R the location coincides with both a steep topographic gradient and the edge of a peculiar jut in the magnetic anomaly pattern (Fig. 1.1). To the north, on the up-fault side, the anomaly is of normal polarity and associated with the Bruhnes epoch; to the south, the anomaly is of reversed

polarity and presumably represents older rocks. In addition, a CSP profile over the topographic high shows evidence of high angle faulting, with negligible vertical offset, from the bottom to the maximum penetration depth of 0.6s two-way time, in approximately the same location as the proposed fault (R.L. Chase, pers. comm., 1975).

No such data is present in the immediate vicinity of the starting point of profile 74-1 to support a fault interpretation. However, the existence of faults for both profiles would be consistent with present ideas regarding the regional tectonics. According to Atwater (1970), the motion of the Juan de Fuca plate relative to the American plate is 2.5 cm/yr toward the northeast, and thus implies subduction. Paul Revere Ridge trends northwest along the northern end of Explorer Ridge and may even be within the subduction zone. Evidence for this is shown by basalts which dip beneath the ridge and sediments which thicken away from the ridge toward the base of the continental slope where they are folded and faulted (Srivastava et al, 1971). If this zone is considered broad enough to include the steep topography which profile 74-1R crossed, a subduction-related fault may be possible.

For profile 74-1 it is noted from Fig. 1.1 that the initial part of the profile is near the northern extent of the Sovanco transform fault zone which joins Juan de Fuca Ridge to Explorer Ridge. As previously mentioned, a reorientation of Explorer Ridge began about 7.5 m.y. ago. The transform faults of the Sovanco fracture zone then

represent "leaky" transform faults (Menard and Atwater, 1969) due to their clockwise rotation (McManus et al, 1972). Thus, a component of vertical offset associated with this process is not unreasonable.

Another result which deserves further attention is the difference in mantle velocities parallel (7.3 km/s) and perpendicular (7.8 km/s) to the ridge crest. The existence of seismic anisotropy in the uppermost mantle is well established (Christensen and Salisbury, 1975) and is the most attractive explanation for these results. In experiments designed to measure the magnitude of anisotropic effects the general conclusion has been that the velocity is a maximum in a direction approximately perpendicular to the ridge and a minimum parallel to it (Raitt et al, 1969; Keen and Barrett, 1971). The work of Keen and Barrett is particularly relevant to this study as it was undertaken in a region farther to the northwest on the Pacific plate. While the overall velocities were higher than those determined here, the magnitude of the anisotropic effect was about 8%. Assuming the velocities determined along the two DSS profiles in this study represent maximum and minimum values, the anisotropic effect is 7%, which compares favorably with the above percentage. This suggests that the anisotropy due to crystal realignment as a result of spreading or flow of "soft" material (Hess, 1964), is "frozen" and completed at or near the ridge. Because the material is younger and warmer in this region the magnitudes of the velocities are

less. As the rocks spread further, they cool, become more compacted and as a result have a higher overall medium velocity. But the anisotropy is maintained as time progresses.

The implications of the seismic models on the petrologic structure of the lower crust/upper mantle is now considered. Because of the lateral discontinuities introduced by the faults of profiles 74-1 and 1R, most attention is given to the models of 74-2 and 2R.

The seismic models imply that a thick (6.9 km), well developed layer 3 unit exists below the ridge crest. A model for the evolution of oceanic crust presented by Cann (1970, 1974) may be relevant for explaining this.

Cann describes the formation of the lower crust in terms of the crystallization of an axial magma chamber. The process actually involves two components. A cumulate layer is formed at the base of the chamber due to fractional crystallization of the magma. At the top of the chamber the magma is cooled by heat conduction through the overlying crust to form an upper unit of isotropic gabbro. The lithological sequence is therefore much the same as the one presented in Sec. 5.1. That is, the layer 3 system will consist, from top to bottom, of unaltered gabbro followed by a layer of cumulate gabbro and finally the Moho which is the boundary between gabbro and peridotite. The boundary between the unaltered gabbro and the cumulates is thought to correspond to the layer 3A-3B seismic boundary (Peterson et al, 1974) which has been detected by Sutton et al (1971).

One explanation for the thick layer 3 unit below Explorer Ridge is, therefore, that it represents such a magma chamber which has cooled since the ridge ceased being an active spreading center. Based on the magnetic anomalies (Brunhes), spreading has occurred in the Explorer area within the last 0.7 m.y. This would imply that a rapid cooling process has taken place in order for the near normal crust to develop at a spreading site. Such a cooling rate may be reasonable, however, since the lack of sediments and increased permeability due to fracturing within the crust (an expected consequence of the internal deformation of Juan de Fuca plate suggested by McManus et al, [1972]) would improve the efficiency of a mechanism such as hydrothermal convection (Lister, 1972) in cooling an axial magma chamber.

A fairly rapid cooling process is also consistent with the fact that no basal layer (layer 3B) was detected on the seismic data. The velocity-depth models of profiles 74-2 and 2R show a nearly constant gradient throughout the lower crust implying that no significant cumulate layer has developed. Or, equivalently, the rapid freezing of the magma chamber has led to a layer 3 composed almost entirely of isotropic gabbro. The sharp increase in the gradient within the final 1 km of the model for 74-2R may perhaps be due to the presence of a thin cumulate layer.

The fact that mantle anisotropy was observed in this study adds support to a peridotite composition for the upper mantle. Olivine is the chief mineral constituent of peridotites and the statistical orientation of olivine

crystals has been regarded as the cause for the widely observed anisotropy in the uppermost mantle (Hess, 1964).

6. CONCLUSION

The significance of utilizing both traveltimes and amplitudes in the interpretation of marine refraction data has been clearly illustrated. The most notable outcome of this approach is the introduction of gradients into the velocity-depth models. Velocity gradients are expected since they reflect variations with depth of density, thermal conditions, and petrology. In general, homogeneous layered models are inadequate for providing a detailed description of the oceanic crust.

Results from the refraction data along the reversed DSS profile perpendicular to Explorer Ridge indicate a total crustal thickness of about 11.5 km near the ridge crest. This was an unexpected result and is atypical of other axial zones. The velocity-depth structure of the 1.4 km sub-bottom material is similar on either side of the ridge, but very different velocity gradients appear in the lower crust (see Fig. 4.11). The velocity of the uppermost mantle is 7.8 km/s in a direction perpendicular to the ridge.

A similar reversed DSS profile recorded parallel to Explorer ridge and 60 km east of it showed some unusual results at either end. Velocities of 7.3 km/s were determined at depths of about 5 km, only 2.6 km sub-bottom. On an offset and delayed branch at greater distances, similar velocities

were calculated. A fault zone with about 5 km of throw is suggested to explain the results (see Fig. 4.11). Additional evidence based on topography and the magnetic anomaly pattern is used to support this hypothesis for the northern end of the profile. Although there is little supporting evidence of this type for the proposed similar feature at the southern end, faulting would be consistent with the tectonic activity that has been suggested for the area. Assuming that the 7.3 km/s material is representative of the upper mantle, an assumption necessitated by data to a distance of 80 km, the total crustal thickness at either end of the profile paralleling Explorer Ridge is about 5.0 km while on the deep side of the fault it is 9.9 km. The latter figure compares only moderately well with the 11.8 km crustal thickness determined for the same region from data along profile 74-2, perpendicular to the ridge. Differences are expected and would be due at least partially to the different velocities which were used in modelling the fault and the cumulative errors which accrue in the calculations.

Variation due to anisotropy is suggested to explain the difference in the upper mantle velocities determined parallel and perpendicular to the ridge. If the calculated values of 7.3 and 7.8 km/s represent the minimum and maximum, respectively, the variation due to anisotropy is about 7%. This compares well with the 8% anisotropic effect determined by Keen and Barrett (1971) in a special study conducted to the northwest. The average velocity of 7.58 km/s for the

uppermost mantle in a region near a ridge crest compares well with the range of velocities determined for crestal areas by other researchers (e.g. LePichon et al, 1965).

The results of this study favor the hypothesis that Explorer Ridge is presently an inactive spreading center. The thick crust determined near the ridge would be a likely consequence of Explorer Ridge being rotated too far from the axis of Juan de Fuca Ridge and thus rendering it inactive. The proposed faults are consistent with the effects of rotation and also the internal deformation occurring within Juan de Fuca plate if an extension of the Queen Charlotte Fault is severing the northwest portion from the remainder of the plate. The fact that anisotropy and magnetic lineations are observed implies that seafloor spreading has occurred in the area and Explorer Ridge was at one time active.

While a number of important conclusions have been made, it is worth noting that an abundance of additional information is contained in the entire suite of seismic data. Additional processing and the interpretation of secondary primary wave and transformed shear wave arrivals may refine the present models. Also, in terms of the interpretation method, a least squares approach to fitting traveltimes and amplitudes would restrict the models more than they could be in this study. Finally, no attention has been given to the near vertical incidence reflection data recorded on these profiles; however, the interpretation of these data would

be invaluable for correlation with the refraction results especially if Moho reflections were observed.

REFERENCES

Atwater, T. 1970. Implications of plate tectonics for the Cenozoic tectonic evolution of western North America. Geol. Soc. Am. Bull. 81, pp. 3513-36.

Barr, S.M. and Chase, R.L. 1974. Geology of the northern end of Juan de Fuca Ridge and sea-floor spreading. Can. J. Earth Sci. 11, pp. 1384-1406.

Bennett, G.T. 1973. A seismic refraction survey along the southern Rocky Mountain Trench. Unpubl. M.Sc. thesis, University of British Columbia.

Bertrand, W.G. 1972. A geological reconnaissance of the Dellwood seamount area, northeast Pacific Ocean, and its relationship to plate tectonics. Unpubl. M.Sc. thesis, University of British Columbia.

Braile, L.W. and Smith, R.B. 1975. Guide to the interpretation of crustal refraction profiles. Geophys. J.R. astr. Soc. 40, pp. 145-176.

Bullen, K.E. 1963. An Introduction to the Theory of Seismology, 3rd ed., Cambridge University Press, New York, 381 pp.

Cann, J.R. 1970. New model for the structure of the ocean crust, Nature 226, pp. 928-30.

_____. 1974. A model for oceanic crustal structure developed. Geophys. J.R. astr. Soc. 39, pp. 169-87.

Červený, V., 1966. On dynamic properties of reflected and head waves in the n-layered Earth's crust. Geophys. J.R. astr. Soc. 11, pp. 139-47.

_____. and Ravindra, R. 1971. Theory of Seismic Head Waves, University of Toronto Press, 312 pp.

Christensen, N.I. 1970. Composition and evolution of the oceanic crust. Mar. Geol. 8, pp. 139-154.

_____. and Salisbury, M.H. 1975. Structure and constitution of the lower oceanic crust. Rev. Geophys. Space Phys. 13, pp. 57-86.

Coleman, R.G. and Irwin, W.P., 1974. Ophiolites and ancient continental margins. In: The Geology of Continental Margins, C.A. Burk and C.L. Drake (Ed.) Springer-Verlag, New York, pp. 921-31.

DeGolyer, E. 1932. The application of seismic methods to submarine geology. Tran. Am. Geophys. Un. 13, pp. 37-40.

Dehlinger, P., Couch, R.W., McManus, D.A. and Gemperle, M. 1970. Northeast Pacific structure. In: The Sea, Part II, A.E. Maxwell (Ed.) Wiley-Interscience, New York, pp. 133-89.

Dobrin, M.B. 1960. Geophysical Prospecting 2nd ed., McGraw-Hill, New York, 446 pp.

Helmberger, D.V. 1968. The crust-mantle transition in the Bering Sea. Bull. Seismol. Soc. Am. 58, pp. 179-214.

_____. and Morris, G.B. 1969. A traveltime and amplitude interpretation of a marine refraction profile: primary waves. J. Geophys. Res. 74, No. 2, pp. 483-94.

_____. and Morris, G.B. 1970. A traveltime and amplitude interpretation of a marine refraction profile: transformed shear waves. Bull. Seismol. Soc. Am. 60, No. 2, pp. 593-600.

Hess, H. 1964. Seismic anisotropy of the uppermost mantle under the oceans. Nature 203, pp. 629-31.

Kanasewich, E.R. 1973. Time Sequence Analysis in Geophysics, University of Alberta Press, 352 pp.

Keen, C.E. and Barrett, D.L. 1971. A measurement of seismic anisotropy in the northeast Pacific. Can. J. Earth Sci. 8, pp. 1056-64.

_____. and Tramontini, C. 1970. A seismic refraction survey on the Mid-Atlantic Ridge. Geophys. J.R. astr. Soc. 20, pp. 473-91.

Kramer, F.S., Peterson, R.A. and Walter, W.C. (Ed.) 1968. Seismic Energy sources 1968 Handbook, United Geophysical Corporation, 57 pp.

LePichon, X., Houtz, R.E., Drake, C.L. and Nafe, J.E. 1965. Crustal structure of the mid-ocean ridges, 1, Seismic refraction measurements. J. Geophys. Res. 70, pp. 319-40.

Lister, C.R.B. 1972. On the thermal balance of a mid-ocean ridge. Geophys. J.R. astr. Soc. 26, pp. 515-35.

Matthews, D.H., Lort, J., Vertue, J., Poster, C.K. and Gass, I.G. 1971. Seismic velocities at the Cyprus outcrop. Nature Phys. Sci. 321, pp. 200-01

McKenzie, D.P. and Morgan, W.J. 1969. Evolution of triple junctions. Nature 224, pp. 125-33.

McManus, D.A., Holmes, M.L., Carson, B., and Barr, S.M. 1972. Late Quaternary tectonics, northern end of Juan de Fuca Ridge (northeast Pacific). Marine Geol. 12, pp. 141-64.

Menard, H.W. and Atwater, T. 1968. Changes in direction of sea-floor spreading. Nature 219, pp. 463-67.

_____. and Atwater, T. 1969. Origin of fracture zone topography. Nature 222, pp. 1037-40.

Minkley, B.G., Tripe, R.L.K. and Healey, D.A. 1970. Oceanographic observations at Ocean Station P (50°N, 145°W) 27 June to 25 September 1969. Fisheries Research Board Canada, Tech. Report 184 222 pp.

Moores, E.M. and Jackson, E.D. 1974. Ophiolites and oceanic crust. Nature 250, pp. 136-38.

Muller, St., Stein A. and Veis, R. 1962. Seismic scaling laws for explosions on a lake bottom. Zeit. f. Geophys. 28, pp. 258-80.

O'Brien, P.N.S. 1960. Seismic energy from explosions. Geophys. J.R. astr. Soc. 3, pp. 29-44.

Peterson, J.J., Fox, P.J. and Schreiber, E. 1974. Newfoundland ophiolites and the geology of the oceanic layer. Nature 247, pp. 194-96.

Poehls, K. 1974. Seismic refraction on the mid-Atlantic Ridge at 37°N. J. Geophys. Res. 79, pp. 3370-73.

Raitt, R.W. 1952. Oceanographic instrumentation. Nat. Res. Council Pub. 309, p. 70.

_____. 1963. The crustal rocks. In: The Sea, M.N. Hill, (Ed.) Interscience, New York, pp. 85-102.

_____., Shor, G.G., Jr., Francis, T.J.G. and Morris, G.B. 1969. Anisotropy of the Pacific upper mantle. J. Geophys. Res. 74, pp. 3095-3109.

Shor, G.G., Jr. 1963. Refraction and reflection techniques and procedure. In: The Sea, M.N. Hill (Ed.) Interscience, New York, pp. 20-38.

Shor, G.G., Jr. and Raitt, R.W. 1969. Explosion seismic refraction studies of the crust and upper mantle in the Pacific and Indian Oceans. In: The Earth's Crust and Upper Mantle, P.J. Hart (Ed.) A.G.U. Mono. 13, pp. 225-30.

Srivastava, S.P., Barrett, D.L., Keen, C.E., Manchester, K.S., Shih, K.G., Tiffin, D.L., Chase, R.L., Thomlinson, A.G., Davis, E.E. and Lister, C.R.B. 1971. Preliminary analysis of geophysical measurements north of Juan de Fuca ridge. Can. J. Earth Sci. 8, pp. 1265-81.

Stacey, R.A. 1973. Gravity anomalies, crustal structure, and plate tectonics, in the Canadian Cordillera. Can. J. Earth Sci. 10, pp. 615-28.

Sutton, G.H., Maynard, G.L. and Hussong, D.M. 1971. Widespread occurrence of a high-velocity basal layer in the Pacific crust found with repetitive sources and sonobuoys. In: The Structure and Physical Properties of the Earth's Crust, J.G. Heacock (Ed.) A.G.U. Mono. 14, pp. 193-209.

Talwani, M., Windisch, C.C. and Langseth, M.G., Jr. 1971. Reykjanes Ridge Crest: A detailed geophysical study. J. Geophys. Res. 76, pp. 473-517.

Tiffin, D.L. and Seeman, D. 1975. Bathymetric map of the continental margin of Western Canada. Open file map, Geol. Surv. Canada.

Tobin, D.G. and Sykes, L.R. 1968. Seismicity and tectonics of the northeast Pacific Ocean. J. Geophys. Res. 72, pp. 3821-46.

Vine, F.J. 1966. Spreading of the ocean floor: New evidence. Science 154, pp. 1405-1415.

_____. and Wilson J.T. 1965. Magnetic anomalies over a young oceanic ridge off Vancouver Island. Science 150, pp. 485-89.

Wiggins, R.A. 1976. Body wave amplitude calculations II. Geophys. J.R. astr. Soc. (submitted for publication).

_____. and Madrid, J.A. 1974. Body wave amplitude calculations. Geophys. J.R. astr. Soc. 37, pp. 423-33.

APPENDIX

FAULT THROW CALCULATIONS

The assumed ray paths for two rays incident on a faulted Moho are shown in the diagram below. One ray is critically refracted along the up-fault interface and produces a head wave arrival at a distance d. The other, slightly steeper ray is refracted into the lower medium and is then critically refracted along the down-fault interface to produce a head wave arrival at a greater distance d´.

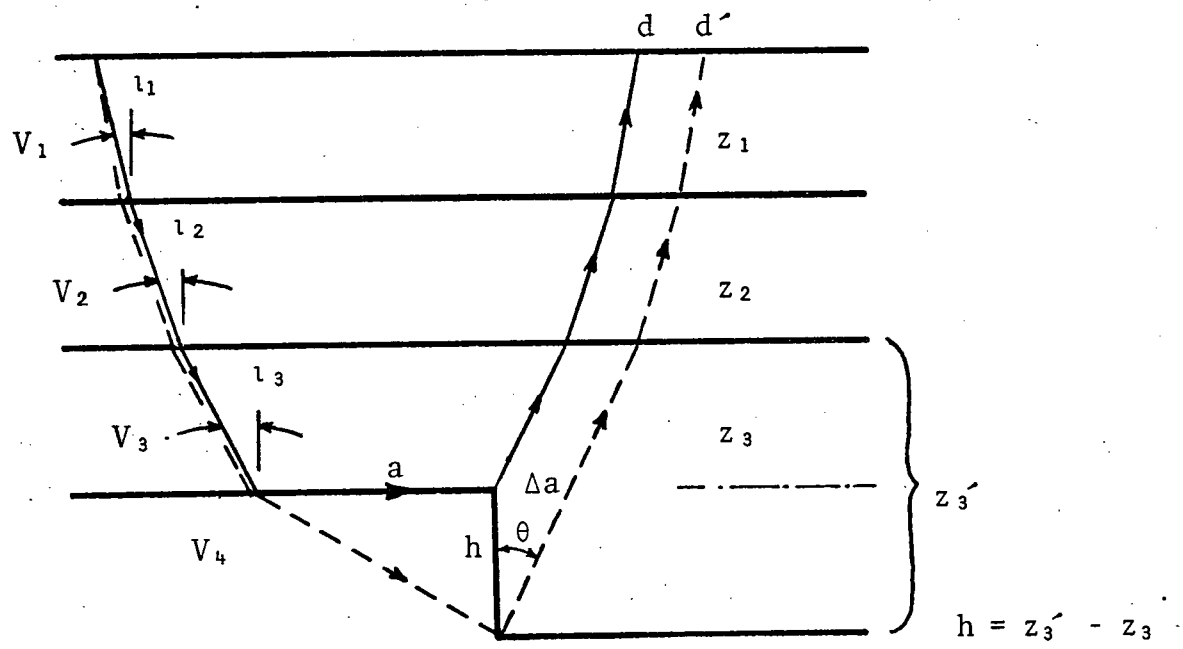

$$\theta = i_{c_3} = \sin^{-1} V_3/V_4$$

In order to consider the traveltime delay due to the fault the traveltimes must be compared at the same receiver distance. Let the distance be d′ for the limiting case. Therefore, the head wave along the up-fault interface must have the quantity $\Delta a/V_4$ added to its traveltime. In terms of the geometry and notation presented in the diagram, the traveltime difference at d′ is

$$\Delta T = \left[\frac{(a^2 + h^2)^{\frac{1}{2}} - a}{V_4} + \frac{h}{V_3 \cos \theta} \right] - \frac{h \tan \theta}{V_4} \qquad \text{Eq. 1}$$

where $a = d - 2z_1 \tan i_1 - 2z_2 \tan i_2 - 2z_3 \tan i_3$.

Using Snell's law the tangents can be expressed in terms of the layer velocities using $\sin i_1 = V_1/V_4$, $\sin i_2 = V_2/V_4$, etc. Thus, the distance a can be expressed as

$$a = d - \frac{2z_1 V_1}{\sqrt{V_4^2 - V_1^2}} - \frac{2z_2 V_2}{\sqrt{V_4^2 - V_2^2}} - \frac{2z_3 V_3}{\sqrt{V_4^2 - V_3^2}} \qquad \text{Eq. 2}$$

Note that if the assumption $a^2 >> h^2$ is made, so that $(a^2 + h^2)^{\frac{1}{2}} \cong a$, ΔT becomes,

$$\Delta T = h \left[\frac{1}{V_3 \cos \theta} - \frac{\tan \theta}{V_4} \right] \qquad \text{Eq. 3}$$

or, by using the fact that $\theta = \sin^{-1} (V_3/V_4)$, this can be written as

$$\Delta T = h \frac{\sqrt{V_4^2 - V_3^3}}{V_3 V_4} \qquad \text{Eq. 4}$$

Eq. 4 is the same as the expression given by Dobrin (1960, p. 81). Since ΔT can be measured from the data, and V_3 and V_4 are known, the fault throw (h) can be easily determined.

To solve Eq. 1 for h without this assumption, the quantity $(a^2 + h^2)^{\frac{1}{2}}$ is first expanded by the binomial theorem. By retaining two terms, the approximation $(a^2 + h^2)^{\frac{1}{2}} \cong a + h^2/2a$ is obtained.

Substituting this result into Eq. 1 gives, after simplyfying,

$$\Delta T = \frac{1}{2aV_4} h^2 + h \left[\frac{1}{V_3 \cos \theta} - \frac{\tan \theta}{V_4} \right]$$

Using Eqs. 3 and 4, this can be written in a standard quadratic form as,

$$\frac{1}{2aV_4} h^2 + \frac{\cos \theta}{V_3} h - \Delta T = 0$$

Solving for h and retaining the positive root, the fault throw can be expressed as

$$h = - a \cot \theta + \sqrt{(a \cot \theta)^2 + 2aV_4 \Delta T} \qquad \text{Eq. 5}$$

where a is given by Eq. 2 and $\cot \theta = \sqrt{\frac{V_4^2 - V_3^2}{V_3}}$

To calculate the fault throw for profiles 74-1 and 74-1R, the following numerical values obtained from the traveltime analysis were used:

Profile 74-1

$V_1 = 1.48$ km/s $\qquad z_1 = 2.40$ km

$V_2 = 4.10$ km/s $\qquad z_2 = 1.80$ km

$V_3 = 5.80$ km/s $\qquad z_3 = 0.90$ km

$V_4 = 7.35$ km/s

$d = 12.5$ km $\qquad \Delta T = 4.67 - 4.10 = 0.57$s

From Eq. 2 the distance a is found to be 6.78 km. Using this in Eq. 5 and making the remaining substitutions, the fault throw becomes h = 3.92 km.

Profile 74-1R

V_1 = 1.48 km/s z_1 = 2.40 km

V_2 = 4.20 km/s z_2 = 1.00 km

V_3 = 6.40 km/s z_3 = 0.90 km

V_4 = 7.24 km/s

d = 20 km ΔT = 4.12 - 3.67 = 0.45s

From Eqs. 2 and 5, the calculated fault throw is h = 4.69 km.

If Eq. 4 had been used instead to calculate h, the fault throw values would be 5.38 km for profile 74-1 and 6.16 km for profile 74-1R.

To calculate the fault throw using HRGLTZ, a quantity ΔT must be found which expresses the difference between the time delay due to the fault (ΔT) and the delay due to increasing the layer thickness by the amount of the fault throw.

For a horizontally layered model based on the up-fault structure the intercept for the Moho refraction branch is

$$T_4 = \sum_{j=1}^{2} 2z_j \frac{(V_4^2 - V_j^2)^{\frac{1}{2}}}{V_j V_4} + 2z_3 \frac{(V_4^2 - V_3^2)^{\frac{1}{2}}}{V_3 V_4}$$

For a model based on the down-fault structure the intercept is

$$T_4' = \sum_{j=1}^{2} 2z_j \frac{(V_4^2 - V_j^2)^{\frac{1}{2}}}{V_j V_4} + 2z_3' \frac{(V_4^2 - V_3^2)^{\frac{1}{2}}}{V_3 V_4}$$

Therefore, by increasing the layer thickness by an amount $h = z'_3 - z_3$, the traveltime is increased by the amount

$$T_4' - T_4 = 2h \frac{(V_4^2 - V_3^2)^{\frac{1}{2}}}{V_3 V_4}$$

The difference $\Delta T = (T_4' - T_4) - \Delta T$ then expresses the amount of time that must be added to the down-fault intercept in the data to produce the down-fault structure with HRGLTZ.

Substituting for $T_4 - T_4'$ and then for h from Eq. 5, the correction ΔT becomes

$$\Delta T = \frac{2 \cos \theta}{V_3} \left[- a \cot \theta + \sqrt{(a \cot \theta)^2 + 2aV_4\Delta T} \right] - \Delta T \qquad \text{Eq. 6}$$

Note that if the expression for h obtained by solving Eq. 4 were used, the result would be much simpler, namely $\Delta T = \Delta T$.

Although velocity gradients were introduced by HRGLTZ, the layer velocities stated above were taken as valid averages for calculating angles. Substituting the numerical data yields ΔT values of 0.261s and 0.235s for profiles 74-1 and 74-1R, respectively. These values represent the amount that the area under the $\Delta(p)$ curve was increased for HRGLTZ and corresponds to depth increases, i.e. fault throws, of 4.5 and 5.1 km for the two profiles.